A Review on the Properties of Iron Aluminide Intermetallics

Mohammad Zamanzade [1,*], Afrooz Barnoush [2] and Christian Motz [1]

[1] Department of Material Science and Methods (MWW), Saarland University, Saarbrücken D-66041, Germany; motz@matsci.uni-sb.de

[2] Department of Engineering Design and Materials, Norwegian University of Science and Technology, Trondheim No-7491, Norway; afrooz.barnoush@ntnu.no

* Correspondence: m.zamanzade@matsci.uni-sb.de; Tel.: +49-681-302-5163; Fax: +49-681-302-5015

Abstract: Iron aluminides have been among the most studied intermetallics since the 1930s, when their excellent oxidation resistance was first noticed. Their low cost of production, low density, high strength-to-weight ratios, good wear resistance, ease of fabrication and resistance to high temperature oxidation and sulfurization make them very attractive as a substitute for routine stainless steel in industrial applications. Furthermore, iron aluminides allow for the conservation of less accessible and expensive elements such as nickel and molybdenum. These advantages have led to the consideration of many applications, such as brake disks for windmills and trucks, filtration systems in refineries and fossil power plants, transfer rolls for hot-rolled steel strips, and ethylene crackers and air deflectors for burning high-sulfur coal. A wide application for iron aluminides in industry strictly depends on the fundamental understanding of the influence of (i) alloy composition; (ii) microstructure; and (iii) number (type) of defects on the thermo-mechanical properties. Additionally, environmental degradation of the alloys, consisting of hydrogen embrittlement, anodic or cathodic dissolution, localized corrosion and oxidation resistance, in different environments should be well known. Recently, some progress in the development of new micro- and nano-mechanical testing methods in addition to the fabrication techniques of micro- and nano-scaled samples has enabled scientists to resolve more clearly the effects of alloying elements, environmental items and crystal structure on the deformation behavior of alloys. In this paper, we will review the extensive work which has been done during the last decades to address each of the points mentioned above.

Keywords: aluminide intermetallics; alloy design; brittleness and ductility; corrosion; oxidation; hydrogen embrittlement

1. Introduction

Transition metal (TM)—aluminide intermetallics including TiAl, NiAl, FeAl and Fe_3Al have unique properties, e.g., high melting points, enhanced oxidation resistance, relatively low density, and can be used as soft magnetic materials [1–7]. Early TM-aluminides have fcc-based crystal structure in contrast to the bcc-based crystal structure of late transition metal alloys. Due to the strongly attractive chemical bonding between the bi-metallic species, they are ordered and have stoichiometry. However, the energy of interatomic bonds differs from the early TM (TiAl, VAl) to the late TM alloys (CoAl, NiAl and FeAl). The calculated heats of formation for aluminides with equiatomic composition are plotted in Figure 1 [8]. The heat of formation is remarkable for the case of Ni aluminides in comparison to the Ti aluminides [9]. However, in both cases Al atoms act as an electron donor. The middle TM aluminides are shown to have much less charge transfer and the lowest degrees of ordering. In the case of late TM alloys, charge transfer from Al to the TM and hybridization between Al sp and transition

metal d-states are the driving force in bonding [8]. Therefore, the Fe-Al neighbors are energetically favored and Al-Al neighbors are avoided.
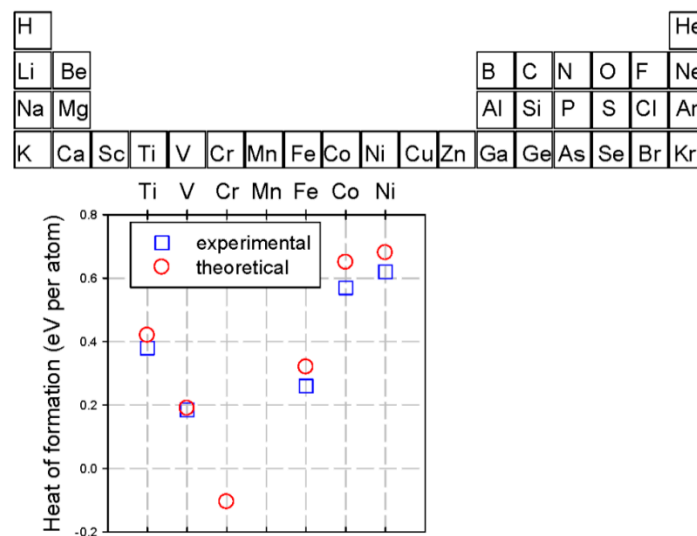

Figure 1. Heats of formation for transition-metal aluminides (with equiatomic composition). Square and circle symbols are experimental and theoretical values, respectively. Re-plotted from the reference [8].

Aluminides were first aimed to be used at high temperatures instead of Ni-based superalloys. Hence, some of the thermo-mechanical properties of the aluminides have been reviewed and compared with the CMSX-4 Ni-based superalloys in Figure 2 [10–13]. The six major advantages of aluminides for high temperature structural applications over the Ni-based superalloys include: (i) higher melting temperatures where the melting temperatures define the upper limit of the service temperature and are indicators of the temperature range at which diffusion-controlled processes start to dominate; (ii) lower densities where the lower densities (especially in the case of γ-TiAl intermetallics) result in lower operating stresses that make it possible to fabricate smaller and lighter components which, in turn, result in better engine accelerations due to the lower mass of the rotating parts; (iii) better oxidation resistance because of the high aluminum content; (iv) lower ductile to brittle transition temperature (DBTT); (v) similar thermal expansion coefficients as the bcc steels and (vi) low costs of production, since they do not generally incorporate rare and strategic elements [10–13]. In contrast, the three negative features of the intermetallics at elevated temperatures are (i) low strength; (ii) limited creep resistance; and (iii) high thermal conductivity. At low to moderate temperatures, most of the intermetallics additionally suffer from poor ductility (Figure 2) and low fracture toughness [14,15]. These problems significantly impede the wide usage of intermetallics because the machining of alloys (at low temperature) becomes very difficult.

Liu *et al.* [16] presented the ductile behavior of aluminides in dry oxygen, where the fracture strain is about 17.6% for Fe-36.5 at. % Al. In general, increasing the Al concentration decreases the density of materials and enhances the protective oxide layer at high temperatures [17,18]. However, the existence of high aluminum concentration has negative side effects [19,20]. The reaction of Al atoms with water results in the production of hydrogen atoms, which are responsible for the low ductility of Fe-Al based intermetallic alloys in moisture-containing atmospheres [21–24] (Figure 3).
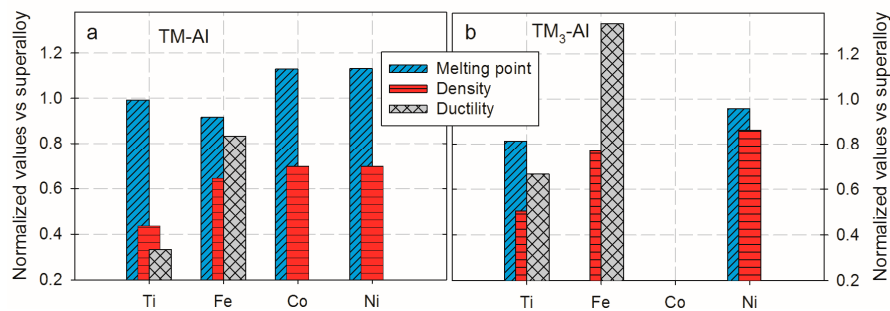
Figure 2. Mechanical properties of transition-metal aluminides [10–13]. (**a**) Equiatomic composition (e.g., 1 Fe:1 Al) and (**b**) three TM: 1 Al compositions. Melting temperature of CMSX-4 Ni-based super-alloy ≈ 1450 °C, Density ≈ 8.70 gr/cm^3, Ductility ≈ 3%.

The rate of a charge-transfer process such as that of hydrogen adsorption depends on the potential across the sample-solution (environment) interface, which can be electrochemically varied in a controlled manner and also by the engineering of the interface. A passive oxide film, for example, causes a drop in the electric current flow. Formation of protective oxide layers on surfaces by pre-oxidizing the iron aluminides may influence the hydrogen adsorption and dissolution in the material and enhance ductility of samples. Furthermore, the thicknesses, crystal structure (if it is amorphous or crystalline), electronic or ionic conductivity, type (if it is n-type or p-type) and numbers of donors in the passive layer may vary based on the alloying elements.
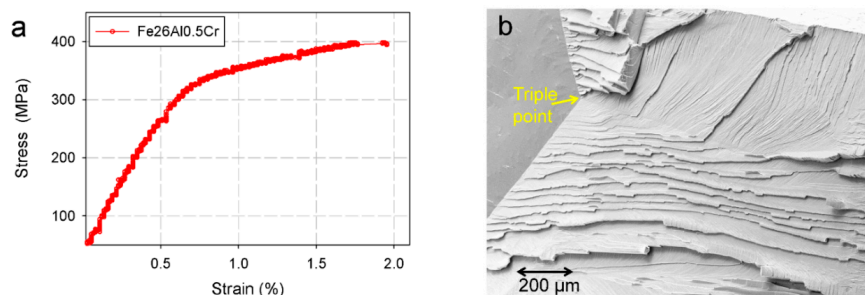

Figure 3. (**a**) Shows low ductility of Fe-Al aluminides; (**b**) Cleavage-like fracture surface of a Fe-26Al-0.5Cr intermetallic after doing tensile test in air. Data from the reference [23].

McKamey *et al.* [25] observed an approximate 8%–10% increase in ductility at room temperature with the addition of 6 at. % chromium. The reasons for the increased ductility after Cr addition are thought to be caused by: (i) the influence of Cr on the bulk properties of binary alloys, such as facilitating the dislocation cross-slipping, solid solution softening and an increment in cleavage strength, and/or (ii) the effect of Cr on the surface properties through the contribution of chromium oxide into the passive layers and the decrement of the kinetics of water reduction reactions, which leads to a reduction of hydrogen formation/adsorption [26–28]. However, the intrinsic complexities of the macro-scale experimental examination make it impossible for us to precisely explore the mechanisms of hydrogen embrittlement in the iron aluminides [29]. In contrast, with the aid of recent local *in-situ* micro-, nano-mechanical testing methods, we can reduce some sources of scatters such as material in-homogeneities during the measurements. Here we will discuss the abilities of *in-situ* nanoindentation measurements [24,29] and *in-situ* compression tests of micro-pillars [22] for evaluating the effects of hydrogen on various mechanical properties such as elastic modulus, dislocation nucleation and mobility. In this review paper, however, it is impossible to develop any of these topics in great detail. Nevertheless, we hope that each section contains enough information for the average reader to understand what has been achieved in that field, as well as satisfactory references to provide further reading if necessary.

2. Characteristics of Fe-Al Intermetallics

2.1. Phase Diagram

The phase diagrams for binary iron aluminides were studied using different techniques, e.g., dilatometric measurement [30], electrical resistivity and specific heat measurement [31], measurement of elastic modulus and magnetic properties [32,33], X-ray diffraction methods [34]; and, more recently, the phase diagram was intensively studied with TEM [35]. The first well-accepted binary Fe-Al phase diagram was reported in 1982 [36]. The phase boundaries and transitional temperatures may differ slightly from one reference to the other. The reason for this uncertainty is the anomaly in the physical properties such as Young's modulus, thermal expansion and electrical resistance. Some possible explanations for the observed irregularities including other long-range ordered states, short-range ordering, two-phase structure, material impurities such as carbide precipitation and quenched-in vacancies are proposed [35,37–39]. The different phases and their lattice structure and lattice parameters are listed in Table 1 [9,40–46].

Table 1. Different Fe-Al phases.

Phase / Liquid	Label in Figure 4	Pearson Symbol	Space Group	Prototype	Lattice Parameters (nm)	Elastic Constants (eV/Å^3)		
Al	Al	$cF4$	$Fm\bar{3}m$	Cu	$a_0 = b_0 = c_0 =$ 0.40496 [43]	$C_{11} = 0.6492,$ $C_{12} = 0.4619$ $C_{44} = 0.2684$ [44]		
$fcc\,(\gamma Fe)$	γFe	$cF4$	$Fm\bar{3}m$	Cu	$a_0 = b_0 = c_0 =$ 0.36599 [40]	–		
$bcc\,(\alpha Fe)$	$A2\,(pm)^*$ $A2\,(fm)^{**}$	$cI2$	$Im\bar{3}m$	W	$a_0 = b_0 = c_0 =$ 0.28665 [43]	$C_{11} = 1.4357,$ $C_{12} = 0.8426$ $C_{44} = 0.73$ [44]		
Fe_3Al	$D0_3$	$cF16$	$Fm\bar{3}m$	BiF_3	$a0 = b0 = c0 =$ 0.2895 [40], 0.5904/2 [44], 0.5792/2 [43]	[44] $C_{11} = 0.945,$ $C_{12} = 0.892,$ $C_{44} = 0.788$	[45] 1.067 0.822 0.815	
$FeAl$	$B2(pm)$	$cP8$	$Pm\bar{3}m$	$CsCl$	$a_0 = b_0 = c_0 =$ 0.291 [41,43,46], 0.283 [9], 0.3031 [44]	[46] $C_{11} = 1.2$ $C_{12} = 0.75$ $C_{44} = 0.73$	[9] 1.8 0.8 1.029	[44] 0.883 0.846 0.691
Fe_5Al_8***	$\varepsilon\,(D8_2)$	$cI52$	$I\bar{4}3m$	Cu_5Zn_8	n.a. [42]	–		
$FeAl_2$	$FeAl_2$	$aP18$	$P1$	$FeAl_2$	$a_0 = 0.4872,$ $b_0 = 0.6459,$ $c_0 = 0.8794,$ $\alpha = 91.76$ $\beta = 73.35,$ $\gamma = 96.89$ [41]	–		
Fe_2Al_5	Fe_2Al_5	$oC?$	$Cmcm$	–	$a_0 = 0.7652,$ $b_0 = 0.6463,$ $c_0 = 0.4229$ [41]	–		
Fe_4Al_{13}	Fe_4Al_{13}	$mC102$	$C2/m$	–	n.a. [41]	–		

* Paramagnetic; ** Ferromagnetic; *** Al-rich intermetallics such as $FeAl_2$, Fe_2Al_5 and Fe_4Al_{13} have lower densities in comparison to FeAl and Fe_3Al but are not good candidates for structural applications because of their small homogeneity ranges, complex crystal structures and brittle behavior. Therefore, we will not focus on them in this text.

Figure 4 [47] shows the extension of the solid solution of Al in Fe from 0 up to 45 at. % Al at high temperatures. At low temperatures, this region is subdivided into three parts. The first part consists of disordered alloys up to 18.75 at. % Al at room temperature. At about 25 at. % Al and temperatures below 545 °C, the intermetallic phase Fe_3Al is formed. The next upcoming phase at higher Al contents is FeAl. Both Fe_3Al (D0$_3$) and FeAl (B2) phases are ordered forms on the body-centered cubic (bcc) lattice and are separated from the disordered A2 phase by first- or second-order transitions.
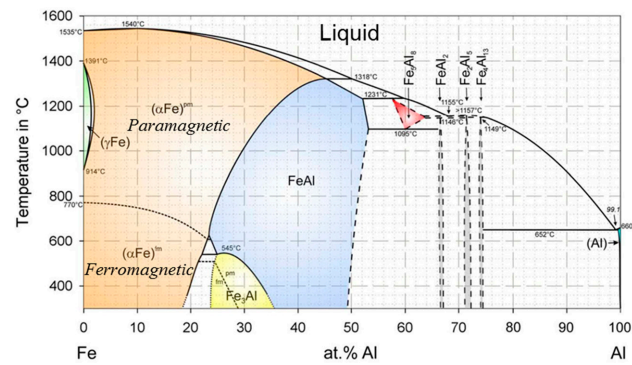
Figure 4. Fe-Al phase diagram. In the phase diagram some of the solubility lines are plotted with dashed lines because they are still not well determined. Data from reference [47].

The X-ray diffraction method was used for studying the distribution of iron and aluminum atoms in the crystal lattice of FeAl (B2) and Fe_3Al (D0$_3$) phases [33,48,49]. The lattice sites in a unit cell are classified into three kinds, α, β and γ as shown in Figure 5a. The probability for each one of these lattice sites to be occupied by an Al atom at room temperature has been plotted against the Al composition, as seen in Figure 5b [48,49]. In the FeAl (B2) crystal lattice, in the stoichiometric composition, Al atoms occupy the body center sublattices (β and γ) and the Fe atoms occupy the corner sites (α sublattice). In the Fe_3Al (D0$_3$) structures, however, the Fe atoms occupy both α and β sublattices, while the Al atoms occupy the γ sublattice. In a D0$_3$ structure, each Fe atom on the α sublattice is surrounded by four Fe and four Al atoms as nearest neighbors (NN), but the Fe atoms on the β sublattice and the Al atoms on the γ sublattice have eight Fe atoms as NNs. This difference significantly influences the defect formation energies [50].

2.2. Point Defects in the Super Cells

The B2 structure has the ideal stoichiometry of 50 at. % Fe-50 at. % Al and the D0$_3$ super structure has the ideal stoichiometry of 25 at. % Fe-75 at. % Al. However, the formation of lattice defects, e.g., vacancies and/or anti-sites, allows for the large range of deviations from the stoichiometric composition. The type and concentration of the point defects are important issues in Fe-Al intermetallics because the constitutional vacancies, or anti-sites, influence the thermo-mechanical, magnetic and electrical properties of the intermetallics. Moreover, the point defects control diffusion-assisted processes, such as creep. The effect of quenched-in thermal vacancies on solid solution strengthening, yield stress and hardness of alloys was studied in detail in the literature we refer to [5,51–54]. It has been shown that vacancies could act as obstacles to dislocation movement. Additionally, strong interactions between structural defect and hydrogen could significantly influence the hydrogen concentration and penetration rates in iron aluminides and cause severe mechanical degradation. Furthermore, the knowledge of point defect energetics is essential for the proper estimation of the formation (excess) energy of extended one-dimensional (1D) or two-dimensional (2D) defects, such as dislocations or grain boundaries, with local off-stoichiometry.
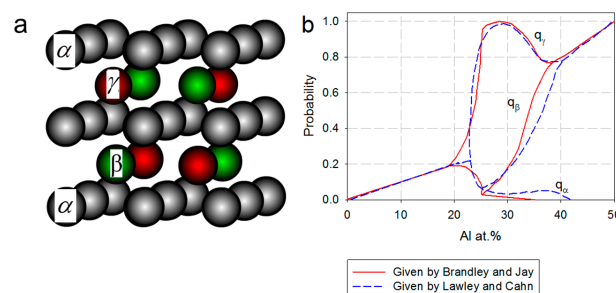

Figure 5. (**a**) Atomic arrangement in a B2 or D0$_3$ super-lattice; (**b**) Occupation probabilities of the lattice sites by Al in a Fe-Al system [48,49].

Point defect structure in intermetallics has been studied extensively with the help of various theoretical methods such as nearest-neighbor pair-wise interactions [55], embedded atom potentials [56] and local-density-functional (LDF) models [57]. The estimated formation energies of different defects in B2 and D0$_3$ super-lattices are presented in Table 2. In a B2 super-lattice, the low formation energies of anti-sites at the Fe and Al sites ($[Fe_{Al}]$ and $[Al_{Fe}]$) and also Fe mono-vacancy ($[V_{Fe}]$) cause high concentrations of these forms of defects. In fact, $[V_{Fe}]$ and $[Al_{Fe}]$ are dominant defect types for Al-rich Fe-Al. For Fe-rich Fe-Al, on the other hand, the constitutional $[Fe_{Al}]$ sites are the main defect type. However, the presence of $[V_{Al}]$ is thermodynamically not favored due to its very high energy of formation.

As it is shown in Table 2, six various forms of point defects could exist on the D0$_3$ sublattices; Fe atoms on the γ sublattice (anti-site Fe atoms), Al atoms on the *α or β* sublattices (anti-site Al atoms) and vacancies on the α, β or γ sublattices. In contrast to the B2 structures, the effective formation energies of all different local defects including vacancies and anti-site atoms vary only slightly with composition in the D0$_3$ structure. However, due to the lower vacancy formation energies in the $[V_{Fe\text{-}α}]$ in comparison with $[V_{Fe\text{-}β}]$, the probability of the $[V_{Fe\text{-}α}]$ is higher. Additionally, the calculated formation energy of $[V_{Al}]$ is not very high; therefore, formation of $[V_{Al}]$ along with $[V_{Fe\text{-}α}]$ is possible.

Along with studying the thermodynamically stable types of defects, the kinetics of defect formation or annihilation are also essential. The A2 crystal structure has a much larger vacancy formation enthalpy, which causes a much lower vacancy concentration compared to the ordered structures (Figure 6a) [39]. The lowest enthalpy and, therefore, the highest concentration of thermal vacancies can be found for the B2 crystal structure [39]. The D0$_3$ structure will have a lower thermal vacancy concentration (in comparison with the B2 structure); it is what we would expect based on the DFE calculations. Most of calculations did not consider the interaction of defects. In reality, however, the vacancy concentrations of both B2 and D03 superlattices are well above the predicted values based on the theoretical calculations. This is due to the interaction of different vacancies and sublattices, which form defect clusters. The higher effective formation volume of the defects in the B2 phases (1.4 Ω), in comparison with one atomic volume Ω, was observed in reference [58]. In the ordered B2 phase, the main defect types are changing from triple defects at low temperature to double vacancies at higher temperature and Al content [58]. In aluminides with less than 35 at. % Al, the type of defects at low temperatures are typically mono-vacancies. Figure 6b [59–62] shows the changes of the equilibrium vacancy concentration (C_v) of samples with different Al contents at different temperatures based on the experimental approaches. Obviously, the increase of either temperature or Al content will increase C_v.

Table 2. The effective formation energies of all different local defects including vacancies and anti-site atoms in eV.

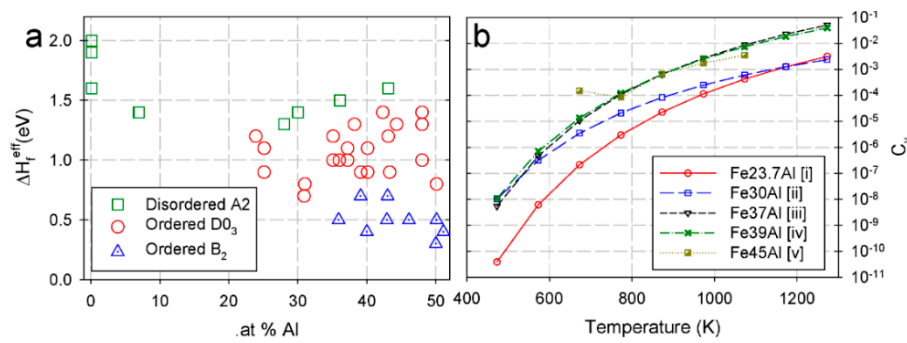| Defects	D0$_3$	B2
$[V_{Fe\text{-}α}]$	1.25 [63], 1.583 [44]	0.97 [57], 1.06, [64], 0.80 [65], 0.653 [66]
$[V_{Fe\text{-}β}]$	2.27 [63], 1.388 [44]	
$[V_{Al}]$	1.4 [63], 2.221 [44]	4.00 [57], 3.46, [64] 2.80 [65], 1.493 [66]
$[Fe_{Al}]$	0.430 [44]	1.03 [57], 0.78[65], 0.95 [66]
$[Al_{Fe\text{-}α}]$	0.047 [44]	0.95 [57], 0.76 [65], 1.03 [66]
$[Al_{Fe\text{-}β}]$	0.218 [44]	

Figure 6. (**a**) Vacancy formation enthalpy for Fe-Al alloys as a function of Al concentration and according to the state of order of the materials [39]; (**b**) Vacancy concentration of Fe-Al alloys based on the experimental approaches (i) [59]; (ii) [60]; (iii) [61]; (iv) [61]; and (v) [62].

The C_v in the materials can be evaluated as follows:

$$C_v = \exp\left[-\frac{\left(E_v^f + pV_v^f - TS_v^f\right)}{k_B T} \right] \tag{1}$$

Where p is the pressure, E_v^f, V_v^f and S_v^f are the energy, volume and entropy of formation of a vacancy, respectively. The migration enthalpy of the defects enhances with increasing Al content; at a constant temperature, the migration of vacancies seems to be very slow, particularly for the high-Al-content alloys. This is because in ordered alloys, unlike in pure metals in which self-diffusion occurs by random vacancy motion, self-diffusion is not possible since it would disrupt the ordering. The possible diffusion mechanisms in the B2 structures are single vacancy transport, triple defects mechanism and the six-jump cycle. The six-jump vacancy model lets diffusion occur exclusively by nearest neighbor vacancy jumps, though diffusion occurs mostly via nearest neighbor jumps into vacant sites. However, both high migration enthalpy and low formation energy of vacancies dictate the existence of large concentrations of thermal vacancies at high temperatures and the quenching of these thermal vacancies is easy.

2.3. Dislocations in Fe-Al

Two slip directions were observed at low temperatures in a B2 super-lattice while the slip plane remains {110}. The slip direction for NiAl and CoAl is <100> while the slip direction for FeAl and Fe₃Al is <111>. The difference between the active slip directions affects the ductility of intermetallics significantly. NiAl and CoAl only have three independent slip systems, which is less than the minimum number of slip systems needed for the plastic flow of material in the polycrystalline materials based on the Von Mises criterion. Therefore, no ductility at room temperature is expected for these alloys. Since the number of slip systems in the Fe-Al intermetallics is more than the required five independent slip systems, iron aluminides are intrinsically ductile. The burgers vector of the B2 iron aluminides is two times longer than that of a normal dislocation in the bcc structure. The super-lattice dislocation splits into two super-partials, each with a $a/2\langle 111\rangle$ burgers vector (b), separated with an anti-phase boundary (APB) [67]. In Fe₃Al with D0₃ structure, a super lattice dislocation with a burgers vector of $\langle 111\rangle$ is known to be dissociated into four super-partial dislocations with $b = a/4\langle 111\rangle$, bound by two types of anti-phase boundaries (APBs): the nearest-neighbor APB (NNAPB) and the next-nearest neighbor APB (NNNAPB) [68]. As it is shown in Figure 7, uncoupled and paired super-partials glide trailing the NNAPB and NNNAPB, respectively. After initiation of the fourth super partial, no APB will be left behind. The surface tension of the NNNAPB after initiation of a $a/4\langle 111\rangle$ may pull back the super-partials during unloading and hence cause pseudo-elasticity. Yasudo *et al.* [69] found a significant shape memory effect in D0₃ alloys with 23 at. % Al for a wide range of temperatures. At this concentration of Al, the super-partials independently glided. The recovery ratio depends on the Al

content and temperature. At 24.7 at. % Al, super-partials moved individually, dragging the NNAPB at room temperature, while at 473 K four-fold dissociated super-dislocations were observed [67,69]. With an Al concentration above 25 at. %, the APB energies increase as long as a homogeneous D0$_3$ structure is present in the Fe-Al phase diagram [70]. At Fe-28.0 at. % Al, a paired super-partial $a/2\langle 111\rangle$ glide and a NNNAPB is left behind [68,71]. Table 3 [72–74] summarizes the energy of NNAPB (γ_{NNAPB}) and NNNAPB (γ_{NNNAPB}) of alloys with different Al content.

The preferred slip plane for both B2 and D0$_3$ is {110}. The frequent short distance double cross-slip processes onto {112}-planes and back onto {110}-planes were observed as well [75,76]. It produces wide slip bands in localized areas at temperatures below 350 K, while adjacent areas remain free of mobile dislocations. The prominent screw character of dislocations was seen, as well as a great number of dipoles in the deformed areas, which resulted from frequent cross-slip events.
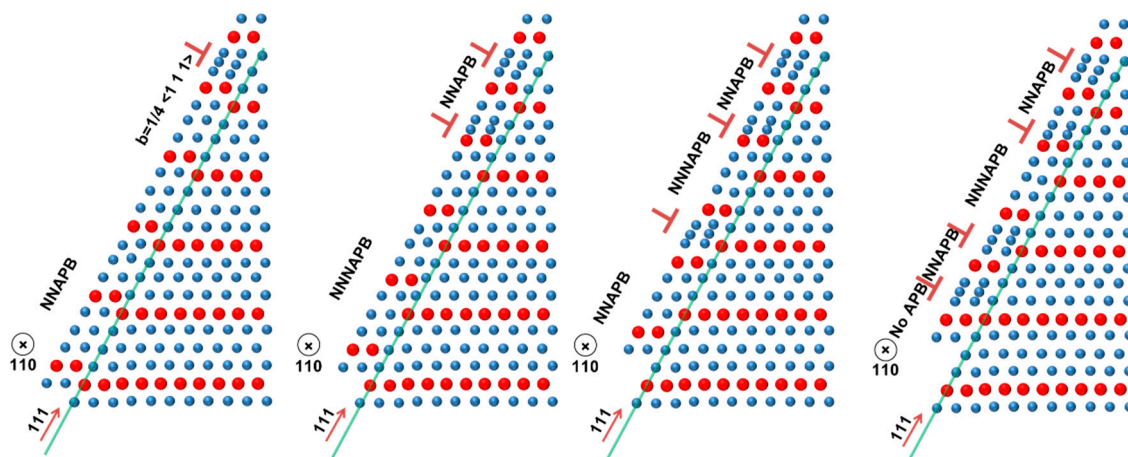

Figure 7. Schematic drawing of the initiation of partial dislocation and formation of anti-phase boundaries in a D0$_3$ super-lattice. Al and Fe atoms are presented in red (bigger) and blue spheres, respectively.

Table 3. The APB energies of D0$_3$ intermetallics at room temperature [72–74].

Alloy (at.%)	γ_{NNAPB}	γ_{NNNAPB}	Ref.
Fe-26.3Al	77 ± 12	85 ± 16	[72]
Fe-26.9Al	68 ± 12	72 ± 13	[73]
Fe-27.8Al	76 ± 11	53 ± 11	[73]
Fe-28Al	73 ± 7	80 ± 7	[74]
Fe-28.3Al	79 ± 10	64 ± 10	[73]

2.4. Mechanical Properties at High Temperatures

The effect of Al content on the yield stress of binary alloys at three different temperatures is presented in Figure 8a [37]. At low to moderate temperatures (T = 773 K), an outstanding enhancement of the yield stress was observed for the D0$_3$ super structure with stoichiometric concentration. Another remarkable mechanical property of iron aluminides is their anomalous increase in yield strength with increasing temperature up to ≈900 K (Figure 8b [77]), which has been observed in single- [78] and polycrystals [79]. There has been much debate about the origin of the observed stress anomaly in the flow stress. It appears to be controlled by several different mechanisms. These mechanisms include anti-phase boundary relaxation leading to dislocation drag, cross-slip of screw dislocations, changing of slip directions from <111> to <001>, super-dislocation climb locking and vacancy hardening [38,39,76,78–80]. Moreover, the Young's modulus of the binary alloys has been studied in detail in a wide range of temperatures (Figure 9) [80,81]. It has been shown that the

Young's modulus of Fe-Al intermetallics with D0$_3$ super structure is minimum at room temperature. The Young's modulus increases with the enhancement of the Al content in each super lattice. It shows the effect of aluminum on the strengthening of the interatomic bonds. Interestingly, the Young's modulus of aluminides with high Al content decreases significantly with the increase of temperature (about 40%), while this decrease is less in the aluminides with less Al content (about 25%).
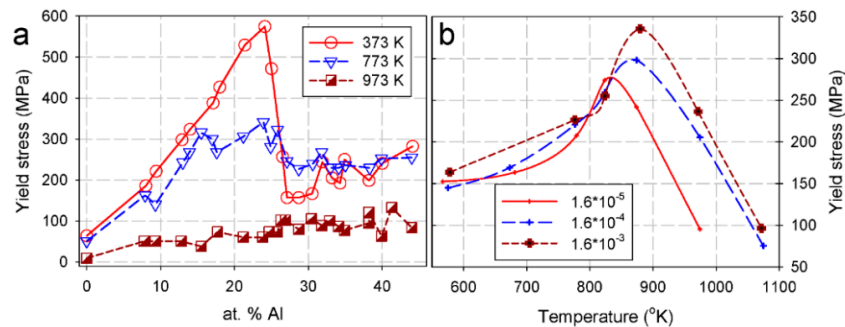

Figure 8. (**a**) Shows the influence of temperature and Al content on the yield stress of binary intermetallics [37]; (**b**) Shows stress anomaly and strain rate sensitivity of Fe-39.5 at. % Al intermetallics for a single slip system–oriented sample [77].
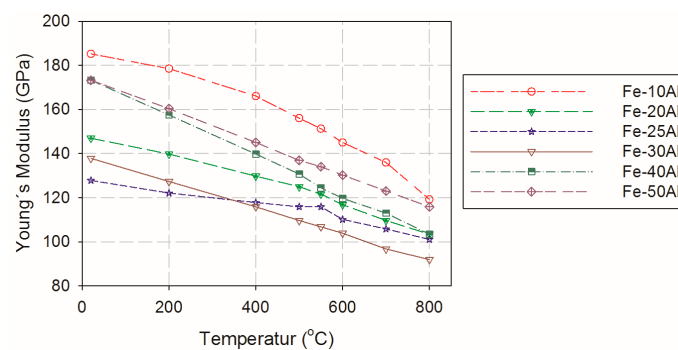

Figure 9. The effect of Al content on the Young's modulus at different temperatures [79,81].

2.5. Alloying Elements

To improve the mechanical, thermal or electrochemical properties of binary Fe-Al intermetallics, one can add some different selected alloying elements to the binary alloys. Some metallic elements such as Si, V, Cr, Mn, Co, Ni, Cu and Zn have large solid solubility [37,82,83] and others such as Zr, Nb and Ta have restricted solid solubility in Fe-Al intermetallics [83,84]. It has been shown that the β sublattice sites are preferred by Ti, W, V, Cr, Mo and Zr whereas Si atoms prefer the γ sublattice in a Fe3Al super-structure [40,85]. The effect of different ternary alloying elements on the formation energies (E_f), relative changes of lattice parameters and Young's modulus were determined using experimental approaches as well as computer simulations (see Table 4) [40,86–88].

The $DO_3 \rightarrow B2$ phase transformation which happens at temperatures of about 550 °C may cause detrimental effects on the mechanical properties [35]. To increase the transition temperature, we can add different ternary alloys such as Nb, Ti, Mo and V. Cr has a very slight effect on temperature transition while V, Mo, Ti and Nb enhance the transitional temperature for 34, 36, 57 and 62 K/at. %, respectively. Furthermore, Stein *et al.* [35] evaluated the effect of two alloying elements on the transition temperature. They found that the two elements may have additive influence at least in the range of studied compositions.

The effects of different alloying elements, namely Cr, Mo, Ti and V, on the solid solution strengthening at various temperatures are summarized in Figure 10 [37]. Increase of the yield stress

relates to the temperature, type and amount of the solute atoms. While Cr does not significantly influence the yield stress at high temperatures, V, Mo and Ti enhance the flow stress about 500%–600% in comparison to the binary alloy at 800 °C.

Table 4. Effect of ternary alloying elements on the properties of Fe_3Al intermetallics.

| –	Formation Energy at Different Sublattices (meV/atom) [40]			Relative Changes of the Lattice Parameter with Respect to the Solute Content	Relative Changes of the Young's Modulus [40]		
	β	α	γ		Theory	Exp. T = 77 K	Exp. T = 300 K
Ti	−242	−191	−194	0.05 [40], 0.03 [88], 0.05 [86]	0.02	0.16	0.17
W	−198	−124	−147	0.03 [40]	0.05	0.13	0.15
V	−229	−182	−188	−0.03 [40], −0.02 [88]	0.04	0.07	0.08
Cr	−185	−175	−156	−0.05 [40], −0.02 [88], 0.01 [86]	0.02	0.02	0.02
Si	−227	−194	−231	–	0.03	0.09	0.08
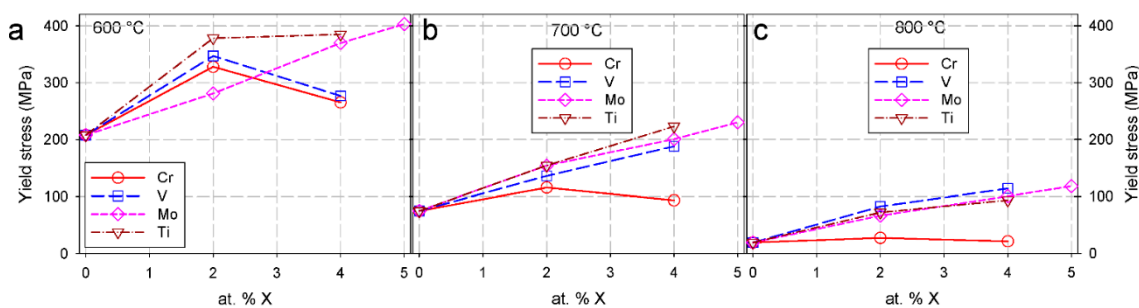
Figure 10. The effect of various ternary alloying elements on the yield stress at (**a**) 600 °C; (**b**) 700 °C; and (**c**) 800 °C [37].

Besides, the addition of low solubility alloying elements (e.g., Nb) may produce precipitates (Fe_2Nb). Niobium is one of the most effective alloying elements in increasing tensile strength at elevated temperatures. Precipitates, which are available in equilibrium in many of the Fe-Al-X systems, have a strong strengthening effect at high temperatures while they prevent grain coarsening but frequently lead to a considerable embrittlement at low or even ambient temperatures [37].

The effects of metallic substitutional atoms, and interstitials, such as boron [89] and carbon [90–92], on the mechanical and corrosion properties of Fe-Al alloys were also studied at different temperatures. Carbon produces plate-like κ-carbide (Fe_3AlC_x) precipitates which are predominantly located along dislocations and grain boundaries [35]. In the Ti-containing alloys, some isolated TiC precipitates were detected as well [35]. Boron could also make dispersoids with solute atoms. Borides can be dispersed in a Fe_3Al matrix after conventional casting methods [93]. Additionally, the thermal stability of Ti, Zr, Ta and Nb diboride precipitates in Fe_3Al-based material was proved earlier [93]. Ti, Hf and Zr diborides lead to significantly improved strengthening at elevated temperatures as well as higher creep resistances (Figure 11a [89]) compared to corresponding binary alloys. Interestingly, the existence of ZrB2 particles has been shown to enhance the strength at 600 °C and also the ductility at room temperature [94]. Maybe the grain structure refinement is the reason for the higher ductility of alloys.

Furthermore, some alloying elements could make stress induce phase transition or form hydride at low temperatures and in moist environments, which may lead to a cleavage-like fracture. The alloys most sensitive to the phase transition in the hydrogen environments are the Ti, Zr, Hf in the IVb column of the periodic table and the V, Nb and Ta in the Vb column of the periodic table. Figure 11b shows the effect of various alloying elements on the brittle to ductile transition temperature (BDTT). It is obvious that many alloying elements have a destructive influence on the ductility at low temperatures and enhance the BDTT temperature.
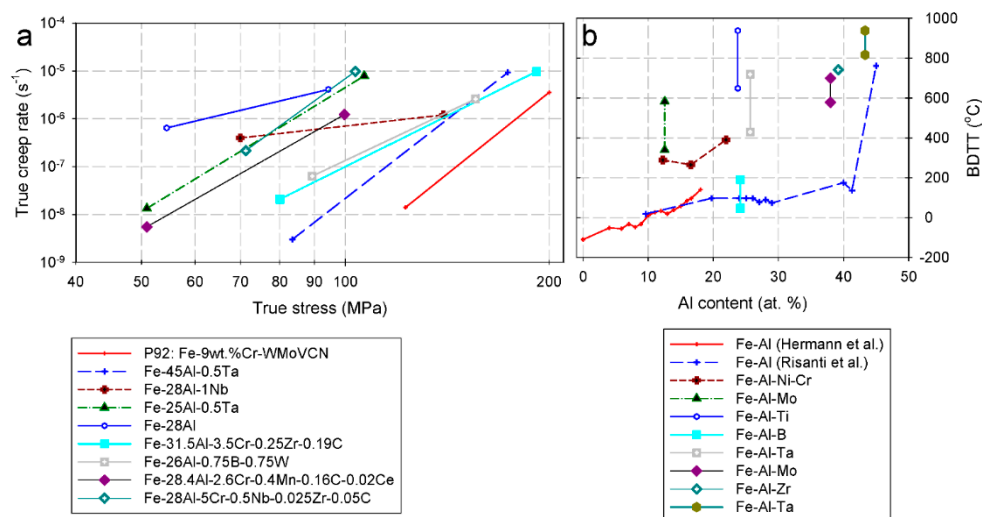
Figure 11. (**a**) Creep rate of various iron aluminides tested at 650 °C [89]; (**b**) Effect of various alloying elements on the brittle to ductile transition temperature (BDTT) [51,95,96].

2.5.1. Influence of Solute Atoms on Mechanical Properties

Anthony and Fultz [97] proposed that the difference of the solute atomic radius compared to the Fe atoms controls their efficiency on the enhancement of transition temperature. However, the contribution of the alloying elements on the valence electron concentration may also play an important role for the transition temperature [88]. In a similar way, according to the classical theories of solid solution strengthening, the difference between solvent and solute atoms in atomic size (atomic size factor) produces local stress fields. It interacts with those of the dislocations, impeding their motion and causing an increase in the macro-hardness or flow stress. Additionally, the modulus misfit is due to the changes of binding energy of atoms after the addition of solute atoms. According to the model proposed by Fleischer [98,99] the magnitude of the solid solution strengthening can be expressed in terms of misfit parameters (ε) based on the following equation [100].

$$\Delta\sigma = \eta M \mu \varepsilon^{1.5} C^{0.5} \tag{2}$$

where η is a constant, M is the Taylor factor and is constant, $\mu = \dfrac{E}{2(1+v)}$ is the shear modulus and C is the concentration of the additional element. The misfit parameters (ε) can be evaluated as follows [100];

$$\varepsilon = \left| \varepsilon'_\mu - \beta\varepsilon_a \right| = \left| \frac{\varepsilon_\mu}{1 + 0.5\left|\varepsilon_\mu\right|} - \beta\varepsilon_a \right| \tag{3}$$

where $\varepsilon_\mu = 1/\mu \times \Delta\mu/\Delta C$ and $\varepsilon_\alpha = 1/a \times \Delta a/\Delta C$ are the modulus misfit parameter and atomic size factor, respectively. However, it is shown that the solid solution strengthening in intermetallics is more complicated compared with binary solutions [100]. For example, the sublattice that the solute atoms prefer to sit on controls the amount of the local stress field. The other complications are the contribution of alloying elements on the phase stability, grain size, energies of anti-phase boundaries and formation/migration enthalpy of the vacancies in B_2 or $D0_3$ structures. Hence, the precise characterization of thermal stability and/or solid solution strengthening in intermetallics requires the consideration of all the aforementioned factors.

2.5.2. Effect of Cr on the Mechanical Properties of Fe-Al Intermetallics

Cr is one of the most important alloying elements and its input on various thermo-mechanical and electrochemical properties has already been studied extensively [23,25,101–104]. Palm experimentally determined an isothermal section for the Fe-Al-Cr system at 1000 °C [82]. He did not find any ternary intermetallic phases because the binary phases can dissolve considerable amounts of the third

component and the substitution does not make any changes in the crystallographic structure. Table 4 summarizes the effect of Cr on lattice constants and Young's modulus. It is shown that the measured Young's and shear modulus increase systematically with the increment of the Cr content in the alloys. The results were interpreted within the framework of the universal features of metallic bonding as a change in the interatomic potential, as proposed by Rose *et al.* [105,106]. The influence of Cr on ordering kinetics and dislocation configurations is not very significant [107]. Furthermore, the effect of Cr on the APBs is also still a matter of debate. While Kral *et al.* [74] found increased APB energy with Cr addition, McKamey *et al.* [25] found that Cr addition reduces the APB energy. Morris *et al.* [75] did not observe differences in the APB energies with Cr addition. Therefore, more experiments and simulations are needed for a precise conclusion about the Cr effect on APB energies.

The effect of Cr content on the incipient plasticity and post-yielding behavior of Fe-26Al-xCr alloys was studied with the aid of different local techniques such as nano-indentation as well as the punching and bending test of micro-pillars [108–110]. Strengthening of the interatomic bonds increases the dislocation line energy, and hence, enhances the energy needed for dislocation nucleation. Furthermore, it has been observed that the addition of 5 at. % Cr increases the nano-hardness at very low depths of indentation and also causes a higher flow stress (yield stress) at low strains in comparison to the binary alloys. This is due to the very low number of available dislocation sources (e.g., Frank-Read sources) in annealed materials [111] in addition to the higher energy needed for dislocation nucleation for Cr-rich alloys [110]. In contrast, at higher strains or depths of indentation, the binary alloy has higher hardness and flow stress (Figure 12). It shows that the amount of strain hardening in the ternary alloy is notably less than that in the binary alloy. It presents the sessile character of dislocations in the binary alloys and the lower ability of dislocations to cross-slip. Postmortem analysis of the nano-indents and punched pillars also proves the effect of Cr on the enhancement of the dislocation mobility, while the height of material pile-ups is decreased around the indents and the slip lines are wide spreading in the Cr-rich alloys [108].
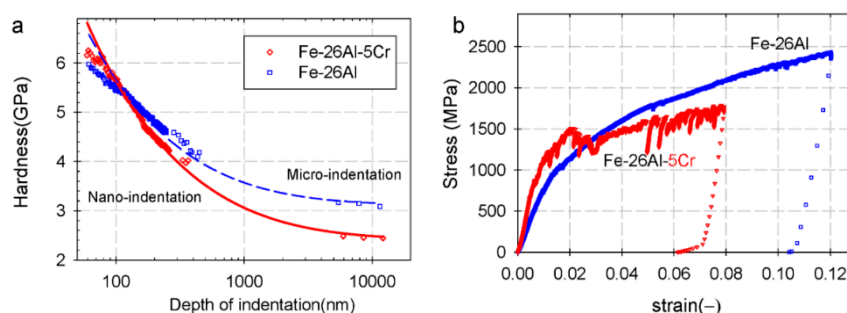

Figure 12. (**a**) The dependence of hardness on indentation depth and Cr content. Data from references [108,109]; (**b**) Stress-strain curves related to the Fe-26Al and Fe-26Al-5Cr micro-pillars. Data from reference [109].

The reduction of average values of material pile-ups after the addition of Cr (Figure 13) could be due to the increase of the capability of the material to include the plastic deformation, *i.e.*, how far dislocations are capable of transferring the plasticity into the material. This can be explained by considering the ease of dislocation cross-slipping in the Cr-rich samples. Additionally, very fine slip steps in the binary alloy (Figure 13e) related to the activation of several crystallographic slip planes were visible. In contrast, due to the localized slip on preferred glide planes, the glide steps of the Cr-containing alloy are well resolved on a few crystallographic planes (Figure 13f).
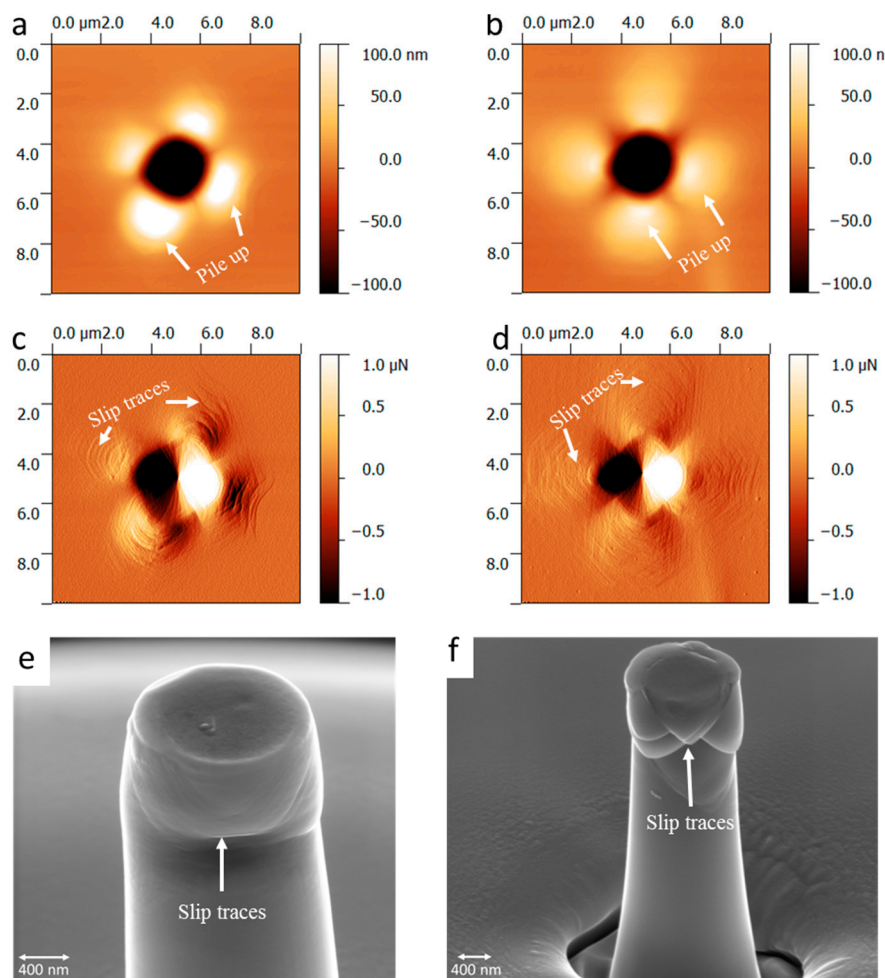
Figure 13. AFM topography and gradient images of material pile-ups for Fe-26Al (**a**) and (**c**) and Fe-26Al-5Cr (**b**) and (**d**). Data from reference [108]. (**e**) and (**f**) represent the slip traces after ~10% strain of Fe-26Al and Fe-26Al-5Cr micro-pillars. Data from reference [109].

3. Environmental Degradation

3.1. Oxidation and Corrosion of Iron-Aluminides

In a binary alloy, one constituent may segregate to the surface while the surface energy is mostly lower than the bulk-terminated alloy surface [112]. Experimental studies on clean, low-index $Fe_{1-x}Al_x$ surfaces show the segregation of Al atoms at the surface. The higher the Al content the more Al exists at the surface. Higher temperatures enhance the Al segregation even more [113,114]. For a stoichiometric Fe_3Al with (110) normal orientation, for example, Al segregation at room temperature was seen to be about 41 at. %, while at 427 °C (below the $D0_3$-B_2 phase transition) the Al content is about 94 at. % within the first layer [115]. It has been shown that the top three layers of atoms may be strongly influenced by surface segregation phenomena and may have a complicated structure [116]. The deviation of the atomic concentration at the surface compared to the bulk material along with the surface energies causes different electronic, chemical and physical properties at the top surface of the samples.

3.1.1. Oxidation Resistance

The Fe-Al intermetallics are aimed to be used in hostile environments, and hence, studying the environmental aspects on the chemical and mechanical properties of alloys is essential. In general,

the oxide growth mechanism consists of two steps; (i) adsorption of oxygen on the metal surface and (ii) formation of an oxide layer, if the coverage of the metallic surface with the oxide layer is energetically favored and no kinetic barriers exist. Once a first oxide layer has formed, it grows further in thickness. Within this second step a charge transfer through the oxide scale is crucial to preserve charge neutrality and therefore further growth. In the studies of the oxidation behavior of B2 aluminides, a parabolic oxide growth rate was observed at high temperatures [117]. It occurs mostly by oxygen diffusing inward through the oxide, with oxide formation taking place at the metal/oxide interface.

The chemical composition of the oxide layer strongly depends on the (i) oxidation rate; (ii) the amount of the alloying elements at the surface; (iii) temperature; (iv) environment or oxidizing media; and (v) the presence of kinetic barriers at the surface. Formation of aluminum oxide is thermodynamically more favorable than iron oxide since oxygen has a higher affinity to Al compared to Fe (the standard Gibbs energy of formation of α-Al_2O_3 is −1,582,260 J/mol which is almost 6.5 times higher compared to FeO). However, the experimental results performed on binary polycrystals (with 15 and 40 at. % Al), oxidized at temperatures around 727 °C in synthetic air, show the existence of a thin Fe_2O_3-containing outer layer followed by an inner, nearly pure Al_2O_3 layer. Additionally, a complex oxide formation (e.g., $AlFeO_3$ or $FeAl_2O_4$ = FeO. Al_2O_3) may happen at low segregation rates of Al from the bulk or high oxidation rates. However, annealing the aluminides at about 1000 °C after oxidation breaks up bonds between Fe and O and leads to the formation of pure Al oxide. In general, at the very beginning of the oxidation process, the oxidation of Fe atoms may happen. After the formation of homogeneous mixed Fe and Al oxides, the supply of oxygen to the metal-oxide interface allows selective oxidation of Al and thereby the development of a continuous film of alumina. The formation of a homogeneous Al_2O_3 layer further slows down oxide growth because electron tunneling remains the only possibility for charge equalization. It may block the Fe oxide formation. Therefore, the existence of a large amount of Al within the surface region in addition to low O_2 pressures in the oxidizing atmosphere causes the formation of pure alumina films. The alumina oxide layer can be either metastable γ-, θ-Al_2O_3, or the slowest-growing, thermodynamically stable α-Al_2O_3, known as corundum. The metastable phases may form at low temperatures (about 700 °C) and transform to the α-Al_2O_3 at high temperatures or after some time. In short, the Fe_2O_3 content decreases with time, temperature and Al concentration of the bulk alloy [118].

The α-Al_2O_3 maintains its desirable oxidation resistance over a wide range of temperatures and in steam environments [119–123]. Increasing the Al concentration enhances the protectivity of the oxide layer at high temperatures [17,18]. A bulk sample with about 14 and 19 at. % Al could maintain its protectivity at temperatures above 800 and 900 °C, respectively [124]. Oxidation resistance of aluminides can be improved by the additions of rare earth metals and transition metals such as Cr, Ti, Nb [37], Y and Ce [125]. However, the addition of high concentrations of Mo or Zr may increase the corrosion rate of iron aluminides (Figure 14) [37]. Additionally, at temperatures higher than 1000 °C, Cr_2O_3 is unstable and its evaporation will increase the oxidation rate of alloys. The addition of small amounts of reactive elements, e.g., Y, Ce, Hf to chromia- and alumina, improves the adhesion of the oxide to the substrate. The presence of alloying elements may limit the outward diffusion of aluminum ions in the oxide layer and, hence, the oxide grows by the inward diffusion of oxygen [126]. On the other hand, alloying elements in the precipitated state may deteriorate the oxidation behavior in terms of internal oxidation. The precipitate-matrix interfaces catalyze the formation of Al_2O_3 and act as starting points for internal oxidation. They are fast paths for oxygen inward and aluminum outward diffusion [124].
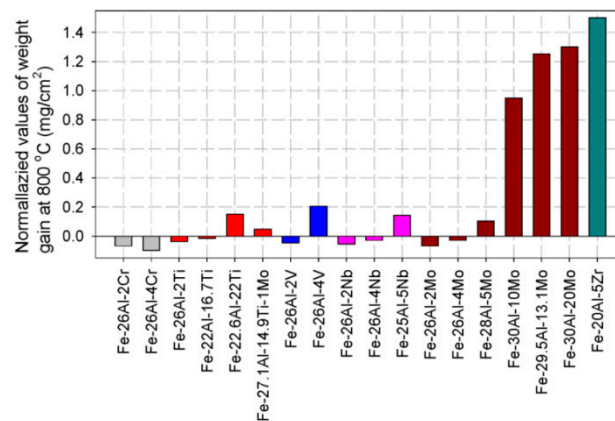
Figure 14. Normalized values of weight gains of Fe-Al-based intermetallics in air (zero line is the mass gain of Fe-26Al) [37].

3.1.2. Electrochemical Properties of Fe-Al Intermetallics

Resistance to aqueous corrosion at low (room) temperatures is essential for the applicability of iron aluminides without compromising their structural integrity. Remarkable enrichment of Al within the passive film [24,127] plays a beneficial role for the passivation of Fe-Al intermetallics. A Pourbaix diagram of aluminum [128] provides information about the thermodynamic stability of different species as a function of potential and pH (Figure 15). At room temperatures and in near-neutral and Cl^--free solutions, aluminum provides a protective insoluble oxide/hydroxide film [129–131]. However, the range of passivity varies with temperature, presence of secondary phases and/or precipitates (in bulk material and/or the oxide layer) and existence of substances in the solution that can form soluble complexes or insoluble salts with aluminum [132,133].
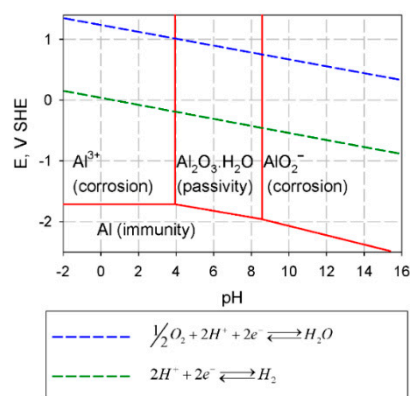

Figure 15. Pourbaix diagram for aluminum at 25 °C.

The contributions of alloying elements on the electrochemical properties of iron aluminides in aqueous environments have rarely been studied. Electrochemical impedance spectroscopy (EIS) and the Mott–Schottky (MS) methods were performed to characterize the passive film of binary and ternary alloys with different Cr content in the near-neutral and Cl^--free solutions [101]. The existence of high donor densities in the passive layers [101] causes semi-conductive behavior. In the sample with a higher concentration of chromium, some part of the iron oxide in the passive layer was replaced by Cr^{3+} Contribution of Cr ions (Cr^{3+} and Cr^{6+}) to the increase of the effective capacitance and donor density of the passive layers was seen based on the electrochemical measurements. The effect of Cr on the polarization resistance was more obvious at high anodic potentials where the strong enrichment of the passive layer with Cr^{3+} and Cr^{6+} could make a more protective p-type passive layer, instead of the

n-type (Al^{3+}-rich) layer, for example at lower potentials or in alloys without Cr [101]. Additionally, it has been shown that the reduction of the flat-band potential after the addition of 5 at. % Cr may reduce the sensitivity of alloys to the moist-induced hydrogen embrittlement [101].

Like other commercial Al-rich alloys, iron-aluminum intermetallics have poor resistance to localized (pitting and crevice) corrosion in Cl^--containing solutions [101,134] (Figure 16 [101]). The incorporation of Cr as a ternary alloying element into the passive film increases the range of passivity and, consequently, the resistance of the alloys to pitting corrosion and decreases the average density of the pits. However, the addition of 5 at. % Cr to the binary Fe_3Al intermetallic does not completely hinder the pitting and crevice corrosion of the alloys. Moreover, the beneficial effect of Si and Ge on the passivating characteristics of Fe_3Al intermetallics has been observed [135]. Zamanzade *et al.* [101] tried to characterize the form and density of (meta) stable pits for different crystal orientations. It was shown that the pit facets have the {110} orientation. The grains with the {110} orientation have slightly higher pit density in comparison with other orientations, but the difference was not significant [101].
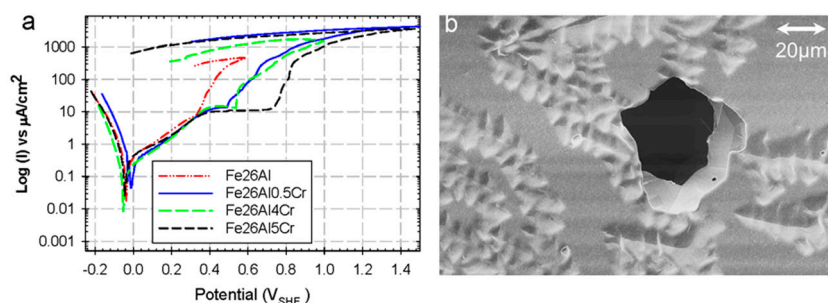

Figure 16. (**a**) Polarization curves show the effect of Cr on the increase of passivation range in a Cl^--containing solution; (**b**) SEM image shows the formation of micro-pits in the iron aluminides. Data from reference [101].

According to the Pourbaix diagram, the corrosion rate increases as the pH moves away from the near-neutral condition. In many acidic solutions, Al dissolves as Al^{3+} ions. In alkaline environments, aluminum dissolves as AlO_2^-. Moreover, like pure aluminum, dissolution of Al_2O_3 may happen due to local alkalization induced by the hydrogen evolution reaction at high cathodic current densities. Al (oxide) dissolution reaction under hydrogen evolution is described as follows [24]:

$$Al_2O_3 + 3H_2O + 2OH^- \rightarrow 2Al\,(OH)_4^- \tag{4}$$

$$Al + 4OH^- \rightarrow Al\,(OH)_4^- + 3e^- \tag{5}$$

3.2. Hydrogen Embrittlement (HE)

Since Johnson [136] first reported on hydrogen embrittlement, various strong views on the mechanisms of hydrogen embrittlement have been vigorously discussed and thoroughly reviewed in the literature. It was shown that hydrogen embrittlement causes severe mechanical degradation of various materials [137,138], especially in aluminides [25,139]. In iron-aluminides, the environmental embrittlement was considered a major cause for the low ductility at ambient temperatures and in air [16,25]. High reactivity of Al atoms with the moisture in air creates hydrogen, and it is the resulting hydrogen atoms that are then responsible for the lowered ductility. At crack tips, this reaction results in embrittlement due to the formation of the atomic hydrogen, which penetrates the material in front of the crack tips.

3.2.1. Mechanism of Hydrogen Ingress

The corrosion of aluminum (Equation (6)) originates the water reduction reaction (Equation (7)) in aqueous environments or moist atmospheres. The consequence of the electro-chemical reactions can be written as follows:

$$Al \rightarrow 3\bar{e} + Al^{3+} \tag{6}$$

$$3 \times \left[H_2O + Al + \bar{e} \rightarrow AlH_{ads} + OH^- \right] \tag{7}$$
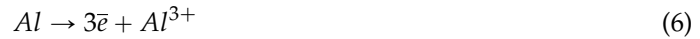
Next, hydrogen is adsorbed (H_{ads}) at the metallic surface as atomic hydrogen. Then, a part of the atomic hydrogen recombines chemically (Tafel reaction (Equation (8)) or electrochemically (Heyrovsky mechanism (Equation (9)) to form molecular hydrogen, H_2, which leaves the metallic surface [140]. The molecular hydrogen does not cause severe embrittlement, possibly as a result of its lower activity in comparison to the atomic hydrogen.

$$AlH_{ads} + AlH_{ads} \rightarrow 2Al + H_2 \tag{8}$$

$$AlH_{ads} + H_2O + e^- \rightarrow Al + H_2 + OH^- \tag{9}$$

A part of H_{ads} will undergo an absorption (H_{abs}) reaction inside the material ($H_{ads} \Leftrightarrow H_{abs}$). The passage of atomic hydrogen through the alloy/solution interface depends on the surface coverage (θ) and also the number of available sites in the subsurface that the hydrogen can occupy. The consequence is the accumulation of hydrogen under the interface, leading to a concentration C_0. Density functional theory's local density approximation calculations [141], in addition to periodic density functional theory calculations within the generalized gradient approximation [142], predicted that hydrogen sits at tetrahedral sites in the bulk Fe-Al lattice, like its interstitial sites in bulk Fe [143]. The activation barrier of some different alloys is presented in Table 5 [142,144,145]. Hydrogen diffusivity in iron-aluminides is lower than in pure Fe (Table 5) [144,146,147]. Electrochemical permeation tests [148–150] found that hydrogen diffusivity in Fe-Al alloys decreases with increasing Al content [146–149,151]. However, new experimental diffusivity data for Fe-Al alloys reported by [149] vary significantly from the older data, presumably due to experimental uncertainties, varying Al concentration, impurities and microstructural differences [142]. Increasing the Cr content of iron [152] or iron aluminum [146] decreases the diffusion coefficient and increases the solubility of hydrogen since the heat of absorption decreases and d-vacancies increase with substitution of Fe with Cr [152].

Table 5. The activation barrier and diffusion coefficient of some different alloys.

Material	Activation Barrier (eV)	Diffusion Coefficient at Room Temperature (m^2/s)
Fe	–	10^{-8}
Fe-18Al	–	10^{-11} [146,148]
Fe-25Al	0.42 [144]	1.45×10^{-13} [146]
Fe-37Al	–	5.57×10^{-10} [149]
Fe-40Al	0.22 [145]	4.4×10^{-13} [147], 5.07×10^{-10} [149]
Fe-43Al	–	4.46×10^{-10} [149]
Fe-46Al	–	3.62×10^{-10} [149]
Fe-50Al	0.26 [142]	2.257×10^{-10} [149]

For the passivated materials, the transport of hydrogen through the passive layer is driven by the electric potential gradient and the hydrogen concentration gradient [153] in contrast to the transport of hydrogen in bulk materials, which is controlled mainly by the concentration gradients. The ionic characteristic of hydrogen atoms (protons) in oxides [154] makes a strong columbic interaction between hydrogen-oxygen ions. It may cause a very high concentration of hydrogen in the oxide in comparison with bulk metal or the metal/oxide interface. For Fe, the ratio of hydrogen concentration in oxide to bulk is measured to be approximately 10^6 [153]. Additionally, the necessity for the breaking of

the columbic bond with the initial oxygen ion causes the mobility of hydrogen in an oxide to be considerably lower than that in the metal phase.

The transport of hydrogen within the oxide must occur by the activated jumping of a proton from one oxygen ion to another [142]. In the case of Fe, for example, the hydrogen diffusivity in the iron oxide layer is much less than that in iron (around 10^{-14} m^2/s) [153,155]. Based on the density functional theory simulation [156], existence of an Al$_2$O$_3$ layer on the Fe-Al bulk material suppresses the mobility of hydrogen atoms. Diffusion of the adsorbed hydrogen atoms from the outer part of the solution/oxide layer into the α-Al$_2$O$_3$ layer is thermodynamically unfavorable, endothermic and rate-controlling. In contrast, the H diffusion from the inner part of α-Al$_2$O$_3$ to the oxide/bulk interface, as well as from the interface into the bulk of the Fe-Al, are thermodynamically spontaneous and exothermic processes [156]. It should be mentioned here that the diffusion mechanism through the passive layer and also the passive layer/bulk metal interface is still largely unknown and has, so far, not been completely explored in published papers. Due to the existence of high donor densities in the passive layers [101], the real thermodynamics and kinetics of hydrogen diffusion may be far from the predicted values based on simulations or the measurements performed on aluminum-rich coatings [157]. The semi-conductive properties of the oxide layer result in a rectification effect, which is the easy movement of current carriers (*i.e.*, electron and protons, H$^+$) from the oxide/electrolyte towards the metal/oxide interface. It eases the reaction of the absorbed H$^+$ ions with the Al substrate at defect sites, which follows with the oxidization of the Al and reduction of H$^+$ [158]. Thus, an increase in hydrogen diffusivity can be expected with an increase in the density of defects and distortion of the long-range order of oxide film.

3.2.2. Hydrogen Interaction with Defects

Along with the conventional hydrogen solubility in the lattice matrix, hydrogen congregates in lattice defects with large surface areas, such as grain boundaries, dislocations, and voids. Point defects such as monovacancies, interstitial atoms and other impurity atoms can also act as hydrogen-trapping defects [159]. The traps are divided into reversible and irreversible or low and high energies, respectively. Table 6 [160–164] shows the strong binding energy of hydrogen at sites near the dislocation core, vacancies and free surfaces.

Table 6. Binding energies of various traps in Fe and Al.

Host Material	Type of Trap	Binding Energy (eV)	Reference (s)
α-Fe	Vacancy	0.63, 0.48	[160,161]
	substitutional (Ti)	0.19	[160]
	interstitial (C)	0.03	[160]
	interstitial (N)	>0.13	[160]
	Grain boundary	0.10	[161]
	Dislocation elastic stress field	0.21	[161]
	Dislocation core	0.61	[161]
	Free surface	0.73	[161]
bcc carbon steel	Fe$_3$C phase interface	0.11	[160]
Al	Vacancy	0.52, 0.53	[160–164]
	Grain boundary	0.15	[160]
	Al$_2$O$_3$-Al phase interface	0.7, 1.0–1.4	[160]

The total hydrogen content in a metal at a defined temperature (C_T^H) is the sum of the solute hydrogen atoms (C_L^H) and the trapped atoms at different defects [143].

$$C_T^H = C_L^H + \sum_j k^H n_j^H N_j^H \tag{10}$$

where k^H is a constant, n_j^H and N_j^H are the fraction of trap sites filled with hydrogen and the total number of trap sites per unit volume, respectively. For the dislocations $N_{dis}^H \approx \pi b^{-1}\rho$, where b and ρ are the burgers vector and dislocation density, respectively. For the grain boundaries, the incomplete information about the atomic arrangement may cause an error in the estimated hydrogen binding energies. However, as a first estimation, we can assume the total number of trap sites per unit volume as $N_{gb}^H \approx b^{-2}L_{gb}$, where L_{gb} is the length of grain boundaries per unit area of observation. Due to the small volume fraction of the metal which is disturbed by the defect, quantification of the interactions between defect and hydrogen may be very difficult. According to Hirth [143], the trapping effect is measureable for a trap density of 10^{23} m^{-3} or more, and is negligible for smaller trap densities at temperatures below 550 K. Dislocation trap densities can exceed this value at room temperature, while recovery decreases the dislocation densities.

The existence of traps also influences the hydrogen diffusion coefficient in different ways. Substitutionally dissolved impurities accelerate the hydrogen diffusion [160], which relates to reduced vacancy formation energy in the excess volume of the boundary. In contrast, the hydrogen diffusion does not rely on vacancies [160]. The mobility of hydrogen can be substantially reduced by its attractive interactions with dislocations. On the other hand, for high purity single-phase single crystals the diffusion paths are either bulk diffusion or pipe diffusion along dislocations [165]. It is possible that the hydrogen does not enter the lattice by diffusion, but is transported into the lattice by gliding dislocations that originate at the surface. The "Cottrell atmosphere", formed around dislocations, could simultaneously move with the dislocation during deformation and improve the transport of hydrogen, if the velocity of the dislocations is less than a critical value [166–168]. The critical velocity (v_c) could be analytically calculated based on the following equation [167]:

$$v_c = \frac{\sigma b l D_{ok}}{RT}\exp\left(-\frac{Q_k + 2F_k^*}{RT}\right) \tag{11}$$

where σ, *l*, *R*, *T*, D_{ok}, Q_k and $2F_k^*$ are applied stress, dislocation length, gas constant, absolute temperature, pre-exponential term for kink diffusion, activation energy for kink diffusion and free energy of formation of a double-kink on a dislocation, respectively. The interaction between hydrogen and dislocations in metals influences not only the hydrogen content and its mobility but also the dislocation motion and plastic flow of material. Hydrogen may suppress the motion of dislocation which reflects the endothermic detrapping necessary to separate the moving dislocations from its hydrogen or, contrarily, the dislocation transport may ease with hydrogen, based on the hydrogen-enhanced local plasticity mechanism.

3.2.3. Hydrogen Embrittlement of Fe-Al Intermetallics

Because of the technological importance of hydrogen embrittlement, many people have explored the nature, causes and control of hydrogen-related degradation of aluminides. There are at least three reasons for the high susceptibility of iron aluminides to hydrogen embrittlement: (i) high reactivity of Al atoms with the moisture in air creates high fugacity of hydrogen atoms; (ii) existence of a high concentration of point defects and especially vacancies (Figure 6b) enhances the solubility of hydrogen in the intermetallics, and increases the influence of hydrogen on the mechanical properties; (iii) the iron aluminides intrinsically have a limited amount of ductility (and very high slip planarity) in comparison to bcc metals, and an additional reduction with hydrogen charging will decrease the ductility even more. The effect of hydrogen on the ductility and crack initiation of iron aluminides was a subject of many studies [169–172]. The polycrystalline Fe-36.5Al was shown to have ductility of just 2.2% in air and 5.4% in vacuum while its ductility in dry oxygen could be as high as 17.6% [16] (Figure 17). However, the fracture of Fe-Al polycrystalline materials seems to be dominated by the intergranular crack growth mechanism in moist environments, while the cracks will grow transgranularly in the Fe$_3$Al structures. For single crystals of Fe-40Al tested in air, crack initiation occurred at the surface and the fracture strain was less than 1%. Specimens tested in an O$_2$ atmosphere had internally initiated

cracks, possibly at flaws, and elongations of ~10% [169–172]. Wittmann *et al.* [165] studied the ductility of Fe-40Al single-slip-oriented single crystals. They also observed improved ductility when tested in vacuum *versus* air, but greater ductility in air (between 1.1%–5.9%) compared with previously reported results for multiple slip-oriented specimens. The elongations and fracture strengths of Fe-40Al single crystals are shown in Table 7 [165]. The scatter, shown in the results, is believed to be due to the small thickness of the tensile specimens. However, the ductility appears to be less in air than in a vacuum. Additionally, higher fracture strengths were seen in a vacuum. Wittmann *et al.* [165] did not observe any differences in environmental embrittlement of specimens oriented in such a way that the strain was predominately carried by screw dislocations or edge dislocations. On the contrary, results from tensile tests of Fe$_3$Al single crystals, oriented in a way that the main strain was produced either by screw dislocations or by edge dislocations, have shown considerable ductility for the screw orientation in both air and vacuum, whereas the edge-oriented specimens showed little ductility in air [171]. Saka and Nishizaki [171] related this difference to the role of edge dislocations in transporting hydrogen into the Fe$_3$Al lattice. The crack in FeAl propagates mainly along the {100} plane in air [169,170]. In contrast, in a vacuum, fracture has been shown to occur along {111} for stoichiometric Fe-Al, and {100} for Fe-40Al, and Fe-35Al [169,170]. Munroe and Baker [173] suggested a concept for HE of iron aluminides. They proposed that the {100} cleavage that results from the interaction of two $a/2\langle 111 \rangle$ edge super-partials may produce a sessile $\langle 100 \rangle$ edge dislocation on {001}. This edge dislocation can then act as a crack nucleus. Moreover, formation of the $\langle 100 \rangle$ edge dislocations may enhance absorption of hydrogen rather than two super-partials [174].

At a constant temperature, and in the absence of any kind of phase transformation (see Section 2.5), the energy of the newly formed surfaces (due to the crack growth) is an intrinsic characteristic of the material. The hydrogen ingress into the materials can reduce the energy needed for formation of new surfaces with decrement of the strength of interatomic bonds, as predicted by the hydrogen-enhanced decohesion (HEDE) mechanism. On the other hand, the presence of hydrogen affects the multiplication or movement of dislocations in agreement with the DEFect ACTing AgeNTS (defactants), adsorption-induced dislocation emission (AIDE), hydrogen-enhanced local plasticity (HELP), *etc.*, theories [24].

However, the magnitude of the influence of hydrogen on each item depends on the alloy content, defect concentrations, temperature, environment, *etc.* In order to clarify the most probable mechanism of hydrogen embrittlement for each material in a defined environmental situation, it is important to resolve the impact of hydrogen separately on each of the mentioned items, which is impossible based on the conventional mechanical testing methods. Hence, the results of macro-mechanical tests present, sometimes, complicated and controversial findings and/or interpretations. In contrast, local techniques enable us to measure the influence of hydrogen on elastic properties, pop-in load and hardness or flow stress, which scale with the strength of interatomic bonds, energy needed for homogeneous dislocation nucleation and mobility of dislocations, respectively [22,24,29]. A very slight reduction of Young's modulus was measured experimentally due to hydrogen charging for intermetallics with different Cr content (Figure 18a) [24]. A 3%–5% reduction of Young's modulus could not explain the high susceptibility of alloys to HE. Moreover, a strong reduction of the energy needed for homogeneous dislocation nucleation (HDN) after hydrogen charging was seen in the binary alloys (Figure 18b [24]). It is probably the main reason for the very high sensitivity of binary alloys to hydrogen embrittlement. The addition of chromium decreases the susceptibility of binary alloys to the HE because the dislocation core radius does not change significantly after hydrogen charging [24]. The increase of the hardness (Figure 18c,d) of alloys after hydrogen charging may be due to the increase of the friction stress of dislocations. All this experimental evidence shows that adsorption of hydrogen will ease dislocation nucleation while the dislocations are less glissile. Therefore, it is proposed that the mechanism of dislocation shielding should be considered for analyzing the fracture characteristics of iron aluminides in atmospheres containing hydrogen [24].
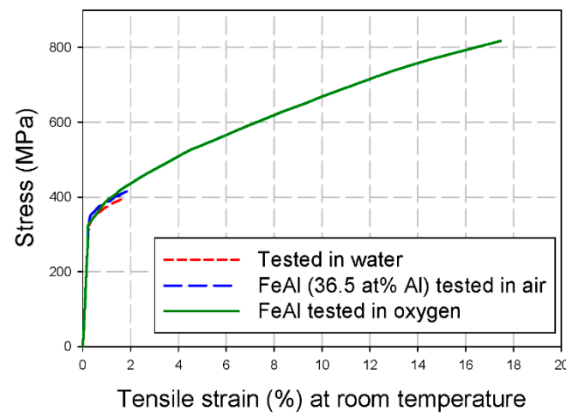
Figure 17. Stress-strain curves of Fe-Al intermetallics in different environments at room temperature. Data from reference [16].
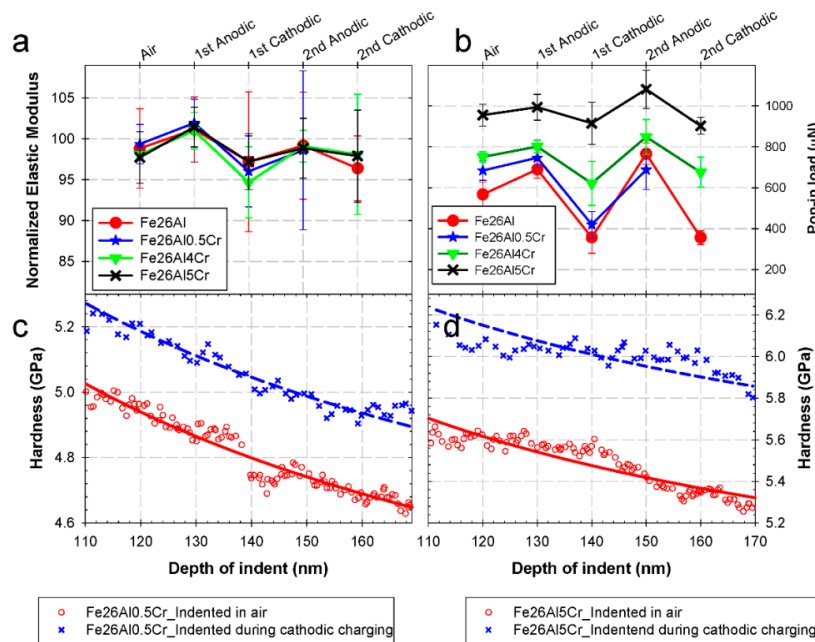

Figure 18. The effect of hydrogen on Young's modulus (**a**); pop-in load (**b**); and hardness (**c** and **d**) for Fe-26Al-xCr alloys. Data from reference [24].

Table 7. Elongation and fracture strength of Fe-40Al in different environments after performing tensile test [165].

Sample Orientation	Elongation (%)		Fracture Strength (MPa)	
	Air	**Vacuum**	**Air**	**Vacuum**
Edge	4.0	9.4	336	460
	3.3	5.7	335	425
	5.9	12.0	320	422
Screw	1.1	3.0	235	435
	2.6	10.8	335	495
	5.7	10.1	345	470

4. Concluding Remarks

This review paper aims to improve the understanding of the factors that control the microstructure and properties of iron aluminides. Some thermo-mechanical behaviors of iron aluminides were studied and compared with super-alloys and stainless steels. Additionally, current applications of the alloys were summarized. The influence of alloying elements on the phase transformation, mechanical properties, corrosion and hydrogen embrittlement were studied. Moreover, the most important barriers for the wide usage of iron aluminides were considered. They include (i) hydrogen embrittlement in the moisture-containing atmospheres at room temperature; (ii) localized corrosion in the Cl$^-$-containing aqueous solutions; (iii) strong reduction of yield stress after a critical temperature; (iv) limited creep resistance; and (v) high thermal conductivity. Finally, possible ways for overcoming these problems were evaluated.

Author Contributions: All authors helped conduct the literature review and prepare the text. Mohammad Zamanzade and Afrooz Barnoush performed electrochemical tests as well as *ex-situ* and *in-situ* nano-indentation measurements. All authors helped to accomplish the tensile tests and micro punching tests of iron aluminides.

Conflicts of Interest: The authors declare no conflict of interest.

References

1. Ziegler, N. Resistance of iron-aluminum alloys to oxidation at high temperatures. *Trans. Am. Inst. Min. Met. Eng.* **1932**, *100*, 267–271.
2. Blau, P.J.; Meyer, H.M. Characteristics of wear particles produced during friction tests of conventional and unconventional disc brake materials. *Wear* **2003**, *255*, 1261–1269. [CrossRef]
3. Judkins, R.R.; Rao, U.S. Fossil energy applications of intermetallic alloys. *Intermetallics* **2000**, *8*, 1347–1354. [CrossRef]
4. Stoloff, N.; Liu, C.; Deevi, S. Emerging applications of intermetallics. *Intermetallics* **2000**, *8*, 1313–1320. [CrossRef]
5. Baker, I.; Munroe, P.R. Mechanical properties of FeAl. *Int. Mater. Rev.* **1997**, *42*, 181–205. [CrossRef]
6. Noebe, R.D.; Bowman, R.R.; Nathal, M.V. Physical and mechanical-properties of the B2 compound nial. *Int. Mater. Rev.* **1993**, *38*, 193–232. [CrossRef]
7. Sundararajan, V.; Sahu, B.R.; Kanhere, D.G.; Panat, P.V.; Das, G.P. Cohesive, electronic and magnetic-properties of the transition-metal aluminides FeAl, CoAl and NiAl. *J. Phys.Condens. Matter* **1995**, *7*, 6019–6034. [CrossRef]
8. Fu, C.L.; Wang, X.D. The effect of electronic structure on the defect properties of FeAl. *Mat. Sci. Eng. A-Struct.* **1997**, *240*, 761–768. [CrossRef]
9. Fu, C.L.; Yoo, M.H. Electronic structure and mechanical behavior of transition-metal aluminides: A first-principles total-energy investigation. *Mater. Chem. Phys.* **1992**, *32*, 25–36. [CrossRef]
10. Miracle, D.; Darolia, R. *NiAl and Its Alloys, Intermetallic Compounds, Vol. 3: Structural Applications of Intermetallic Compounds*; Wiley: New York, NY, USA, 1994.
11. Huang, S.C.; Chesnutt, C.J. *Gamma TiAl and Its Alloys, Intermetallic Compounds, Vol. 3: Structural Applications of Intermetallic Compounds*; Wiley: New York, NY, USA, 1994.
12. Briant, C.L. *Intergranular and Cleavage Fracture, Intermetallic Compounds, Vol. 2: Basic Mechanical Properties and Lattice Defects of Intermetallic Compounds*; Wiley: New York, NY, USA, 1994.
13. Vedula, K. *FeAl and Fe$_3$Al, Intermetallic Compounds, Vol. 3: Structural Applications of Intermetallic Compounds*; Wiley: New York, NY, USA, 1994.
14. Mckamey, C.G.; Devan, J.H.; Tortorelli, P.F.; Sikka, V.K. A review of recent developments in Fe$_3$Al-based alloys. *J. Mater. Res.* **1991**, *6*, 1779–1805. [CrossRef]
15. Liu, C.T. Recent advances in ordered intermetallics. *Mater. Chem. Phys.* **1995**, *42*, 77–86. [CrossRef]
16. Liu, C.; Lee, E.; McKamey, C. An environmental effect as the major cause for room-temperature embrittlement in FeAl. *Scr. Metall. Mater.* **1989**, *23*, 875–880. [CrossRef]
17. Prescott, R.; Graham, M. The oxidation of iron-aluminum alloys. *Oxid. Metals* **1992**, *38*, 73–87. [CrossRef]

18. Tortorelli, P.; Natesan, K. Critical factors affecting the high-temperature corrosion performance of iron aluminides. *Mater. Sci. Eng.: A* **1998**, *258*, 115–125. [CrossRef]

19. Alven, D.; Stoloff, N. The influence of composition on the environmental embrittlement of Fe$_3$Al alloys. *Mater. Sci. Eng.: A* **1997**, *239*, 362–368. [CrossRef]

20. Castagna, A.; Stoloff, N. Hydrogen embrittlement of Fe$_3$Al alloys. *Mater. Sci. Eng. A* **1995**, *192*, 399–406. [CrossRef]

21. Balasubramaniam, R. Hydrogen in iron aluminides. *J. Alloys Compd.* **2002**, *330*, 506–510. [CrossRef]

22. Barnoush, A.; Dake, J.; Kheradmand, N.; Vehoff, H. Examination of hydrogen embrittlement in FeAl by means of *in situ* electrochemical micropillar compression and nanoindentation techniques. *Intermetallics* **2010**, *18*, 1385–1389. [CrossRef]

23. Zamanzade, M.; Barnoush, A. An overview of the hydrogen embrittlement of iron aluminides. *Procedia Mater. Sci.* **2014**, *3*, 2016–2023. [CrossRef]

24. Zamanzade, M.; Vehoff, H.; Barnoush, A. Cr effect on hydrogen embrittlement of Fe$_3$Al-based iron aluminide intermetallics: Surface or bulk effect. *Acta Mater.* **2014**, *69*, 210–223. [CrossRef]

25. McKamey, C.; Horton, J.; Liu, C. Effect of chromium on properties of Fe$_3$Al. *J. Mater. Res.* **1989**, *4*, 1156–1163. [CrossRef]

26. Keddam, M.; Mattos, O.; Takenouti, H. Mechanism of anodic dissolution of iron-chromium alloys investigated by electrode impedances—I. Experimental results and reaction model. *Electrochim. Acta* **1986**, *31*, 1147–1158. [CrossRef]

27. Keddam, M.; Mattos, O.; Takenouti, H. Mechanism of anodic dissolution of iron-chromium alloys investigated by electrode impedances—II. Elaboration of the reaction model. *Electrochim. Acta* **1986**, *31*, 1159–1165. [CrossRef]

28. Epelboin, I.; Keddam, M.; Mattos, O.; Takenouti, H. The dissolution and passivation of Fe and Fe-Cr alloys in acidified sulphate medium: Influences of pH and Cr content. *Corros. Sci.* **1979**, *19*, 1105–1112. [CrossRef]

29. Barnoush, A.; Vehoff, H. Recent developments in the study of hydrogen embrittlement: Hydrogen effect on dislocation nucleation. *Acta Mater.* **2010**, *58*, 5274–5285. [CrossRef]

30. McQueen, H.J.; Kuczynski, G.C. Order-disorder transformations in iron-aluminum alloys. *Trans. Am. Inst. Min. Metall. Eng.* **1959**, *215*, 619–622.

31. Eguchi, T.; Matsuda, H.; Oki, K.; Kiyoto, S.-i.; Yasutake, K. Order-disorder transformation in Fe-Al alloys. *Trans. Jpn. Inst. Metals* **1967**, *8*, 174–179. [CrossRef]

32. Koster, W.; Godecke, T. Physical measurements on iron—Aluminum alloys between 10 and 50 at.% Al. I.—Confirmation of and additional conribution to the iron—Aluminum phase diagram. *Z. Metallkd.* **1980**, *71*, 765–769.

33. Taylor, A.; Jones, R. Constitution and magnetic properties of iron-rich iron-aluminum alloys. *J. Phys. Chem. Solids* **1958**, *6*, 16–37. [CrossRef]

34. Davies, R. An X-ray and dilatometric study of order and the "k-state" in iron-aluminum alloys. *J. Phys. Chem. Solids* **1963**, *24*, 985–992. [CrossRef]

35. Stein, F.; Schneider, A.; Frommeyer, G. Flow stress anomaly and order–disorder transitions in Fe$_3$Al-based Fe-Al-Ti-X alloys with X = V, Cr, Nb, or Mo. *Intermetallics* **2003**, *11*, 71–82. [CrossRef]

36. Kubaschewski, O. *Iron-Binary Phase Diagrams*; Springer: Berlin, Germany, 1982.

37. Palm, M. Concepts derived from phase diagram studies for the strengthening of Fe-Al-based alloys. *Intermetallics* **2005**, *13*, 1286–1295. [CrossRef]

38. Morris, D.; Liu, C.; George, E. Pinning of dislocations and the origin of the stress anomaly in FeAl alloys. *Intermetallics* **1999**, *7*, 1059–1068. [CrossRef]

39. Morris, D.G.; Munoz-Morris, M. The stress anomaly in FeAl-Fe$_3$Al alloys. *Intermetallics* **2005**, *13*, 1269–1274. [CrossRef]

40. Friák, M.; Deges, J.; Krein, R.; Frommeyer, G.; Neugebauer, J. Combined ab initio and experimental study of structural and elastic properties of Fe$_3$Al-based ternaries. *Intermetallics* **2010**, *18*, 1310–1315. [CrossRef]

41. Palm, M.; Inden, G.; Thomas, N. The Fe-Al-Ti system. *J. Phase Equilib.* **1995**, *16*, 209–222. [CrossRef]

42. Ducher, R.; Stein, F.; Viguier, B.; Palm, M.; Lacaze, J. A re-examination of the liquidus surface of the Al-Fe-Ti system. *Z. Metallkd.* **2003**, *94*, 396–410. [CrossRef]

43. Calvert, L.; Villars, P. *Pearson's Handbook of Crystallographic Data for Intermetallic Phases*; ASM International: Materials Park, OH, USA, 1991.

44. Shu, X.L.; Hu, W.Y.; Xiao, H.N.; Deng, H.Q.; Zhang, B.W. Vacancies and antisites in B2 FeAl and D0$_3$ Fe$_3$Al with a modified analytic eam model. *J. Mater. Sci. Technol.* **2001**, *17*, 601–604.

45. Leamy, H.; Gibson, E.; Kayser, F. The elastic stiffness coefficients of iron-aluminum alloys-I experimental results and thermodynamic analysis. *Acta Metall. Mater.* **1967**, *15*, 1827–1838. [CrossRef]

46. Vailhe, C.; Farkas, D. Shear faults and dislocation core structure simulations in B2 FeAl. *Acta Mater.* **1997**, *45*, 4463–4473. [CrossRef]

47. Stein, F. Summer School on Iron Aluminides Part 1: The binary Fe-Al system. In Proceedings of the 5th Discussion Meeting on the Development of Innovative Iron Aluminum Alloys in Prague, Prague, Czech Republic, 21–24 September 2009.

48. Bradley, A.; Jay, A. The formation of superlattices in alloys of iron and aluminium. *Proc. R. Soc. Lond. Ser. A* **1932**, 210–232. [CrossRef]

49. Lawley, A.; Cahn, R. A high temperature X-ray study of ordering in iron-aluminium alloys. *J. Phys. Chem. Solids* **1961**, *20*, 204–221. [CrossRef]

50. Fu, C.L. Origin of ordering in B2-type transition-metal aluminides: Comparative study of the defect properties of PdAl, NiAl, and FeAl. *Physical Review B* **1995**, *52*, 3151–3158. [CrossRef]

51. Herrmann, J.; Inden, G.; Sauthoff, G. Deformation behaviour of iron-rich iron-aluminum alloys at low temperatures. *Acta Mater.* **2003**, *51*, 2847–2857. [CrossRef]

52. Herrmann, J.; Inden, G.; Sauthoff, G. Deformation behaviour of iron-rich iron-aluminium alloys at high temperatures. *Acta Mater.* **2003**, *51*, 3233–3242. [CrossRef]

53. Hasemann, G.; Schneibel, J.H.; George, E.P. Dependence of the yield stress of Fe$_3$Al on heat treatment. *Intermetallics* **2012**, *21*, 56–61. [CrossRef]

54. Hasemann, G.; Schneibel, J.H.; Krüger, M.; George, E.P. Vacancy strengthening in Fe$_3$Al iron aluminides. *Intermetallics* **2014**, *54*, 95–103. [CrossRef]

55. Neumann, J.; Chang, Y.; Lee, C. Thermodynamics of intermetallic phases with the triple-defect B2 structure. *Acta Metall. Mater.* **1976**, *24*, 593–604. [CrossRef]

56. Foiles, S.; Daw, M. Application of the embedded atom method to Ni$_3$Al. *J. Mater. Res.* **1987**, *2*, 5–15. [CrossRef]

57. Fu, C.; Ye, Y.-Y.; Yoo, M.; Ho, K. Equilibrium point defects in intermetallics with the B2 structure: NiAl and FeAl. *Phys. Rev. B* **1993**, *48*, 6712. [CrossRef]

58. Stein, F.; Palm, M. Re-determination of transition temperatures in the Fe-Al system by differential thermal analysis. *Int J. Mater. Res.* **2007**, *98*, 580–588. [CrossRef]

59. Schaefer, H.-E.; Frenner, K.; Würschum, R. High-temperature atomic defect properties and diffusion processes in intermetallic compounds. *Intermetallics* **1999**, *7*, 277–287. [CrossRef]

60. Hehenkamp, T.; Scholz, P.; Köhler, B.; Kerl, R. Vacancy formation and diffusion in FeAl-alloys. *Defect Diffus. Forum* **2001**, *194–199*, 389–396. [CrossRef]

61. Würschum, R.; Grupp, C.; Schaefer, H.-E. Simultaneous study of vacancy formation and migration at high temperatures in B2-type Fe aluminides. *Phys. Rev. Lett.* **1995**, *75*, 97. [CrossRef] [PubMed]

62. Schneibel, J. Strengthening of iron aluminides by vacancies and/or nickel. *Mater. Sci. Eng. A* **1998**, *258*, 181–186. [CrossRef]

63. Mayer, J.; Meyer, B.; Oehrens, J.S.; Bester, G.; Börnsen, N.; Fähnle, M. Effective formation energies of atomic defects in D0$_3$ Fe$_3$Al: An ab-initio study. *Intermetallics* **1997**, *5*, 597–600. [CrossRef]

64. Fähnle, M.; Mayer, J.; Meyer, B. Theory of atomic defects and diffusion in ordered compounds, and application to B2-FeAl. *Intermetallics* **1999**, *7*, 315–323. [CrossRef]

65. Besson, R.; Morillo, J. Development of a semiempirical n-body noncentral potential for Fe-Al alloys. *Phys. Rev. B* **1997**, *55*, 193–204. [CrossRef]

66. Bakker, H.; Modder, I.; Kuin, M. Extension of miedema's semiempirical model to estimates of the formation enthalpies of point defects in intermetallic compounds with the B2 structure. *Intermetallics* **1997**, *5*, 535–546. [CrossRef]

67. Yasuda, H.Y.; Umakoshi, Y. Pseudoelastic behaviour of Fe$_3$Al single crystals with D0$_3$ structure. *Intermetallics* **2010**, *18*, 1273–1278. [CrossRef]

68. Yasuda, H.; Nakajima, T.; Nakano, K.; Yamaoka, K.; Ueda, M.; Umakoshi, Y. Effect of Al concentration on pseudoelasticity in Fe$_3$Al single crystals. *Acta Mater.* **2005**, *53*, 5343–5351. [CrossRef]

69. Yasuda, H.Y.; Nakajima, T.; Umakoshi, Y. Temperature dependence of pseudoelasticity in Fe$_3$Al single crystals. *Intermetallics* **2007**, *15*, 819–823. [CrossRef]

70. Wolff, J.; Franz, M.; Hehenkamp, T. Defect analysis with positron annihilation-Applications to Fe aluminides. *Microchim. Acta* **1997**, *125*, 263–268. [CrossRef]

71. Saburi, T.; Yamauchi, I.; Nenno, S. Electron microscope observation of dislocations and antiphase boundaries in iron-aluminum alloys. *J. Phys. Soc. Jpn.* **1972**, *32*, 694–701. [CrossRef]

72. Crawford, R.C.; Ray, I.L.F.; Cockayne, D.J. Weak-beam technique applied to superlattice dislocations in iron-aluminum alloys. 2. Fourfold dissociation in D0$_3$-type order. *Philos. Mag.* **1973**, *27*, 1–7. [CrossRef]

73. Crawford, R.C.; Ray, I.L.F. Antiphase boundary energies in iron-aluminum alloys. *Philos. Mag.* **1977**, *35*, 549–565. [CrossRef]

74. Král, F.; Schwander, P.; Kostorz, G. Superdislocations and antiphase boundary energies in deformed Fe$_3$Al single crystals with chromium. *Acta Mater.* **1997**, *45*, 675–682. [CrossRef]

75. Morris, D.; Dadras, M.; Morris, M. The influence of cr addition on the ordered microstructure and deformation and fracture behaviour of a Fe 28% Al intermetallic. *Acta Metall. Mater.* **1993**, *41*, 97–111. [CrossRef]

76. Brinck, A.; Engelke, C.; Neuhäuser, H.; Molénat, G.; Rösner, H.; Langmaack, E.; Nembach, E. Dislocation processes in Fe$_3$Al investigated by transmission electron, scanning force and optical microscopy. *Mater. Sci. Eng. A* **1998**, *258*, 32–36. [CrossRef]

77. Yoshimi, K.; Hanada, S.; Yoo, M. Yielding and plastic flow behavior of B2-type Fe-39.5 mol.% Al single crystals in compression. *Acta Metall. Mater.* **1995**, *43*, 4141–4151. [CrossRef]

78. Schröer, W.; Hartig, C.; Mecking, H. Plasticity of D0$_3$-ordered Fe-Al and Fe-Al-Si single-crystals. *Z. Metallkd.* **1993**, *84*, 294–300.

79. Yoo, M.; Koeppe, M.; Hartig, C.; Mecking, H.; Hermann, W.; Sockel, H.-G. Effect of temperature on elastic constants and dislocation properties of Fe 30% Al single crystals. *Acta Mater.* **1997**, *45*, 4323–4332. [CrossRef]

80. Yoo, M.; Horton, J.; Liu, C. Micromechanisms of yield and flow in ordered intermetallic alloys. *Acta Metall. Mater.* **1988**, *36*, 2935–2946. [CrossRef]

81. Koster, W.; Godecke, T. Physical measurements on iron-aluminium alloys between 10 and 50 at.-% Al. Iv.—The modulus of elasticity of the alloys. *Z. Metallkd.* **1982**, *73*, 111–114.

82. Palm, M. The Al-Cr-Fe system–phases and phase equilibria in the Al-rich corner. *J. Alloys Compd.* **1997**, *252*, 192–200. [CrossRef]

83. Alonso, P.R.; Gargano, P.H.; Bozzano, P.B.; Ramírez-Caballero, G.E.; Balbuena, P.B.; Rubiolo, G.H. Combined ab initio and experimental study of A2 + L2$_1$ coherent equilibria in the Fe-Al-X (X = Ti, Nb, V) systems. *Intermetallics* **2011**, *19*, 1157–1167. [CrossRef]

84. Stein, F.; Sauthoff, G.; Palm, M. Phases and phase equilibria in the Fe-Al-Zr system: Dedicated to professor dr. Peter neumann on the occasion of his 65th birthday. *Z. Metallkd.* **2004**, *95*, 469–485. [CrossRef]

85. Fu, C.L.; Zou, J. Site preference of ternary alloying additions in FeAl and NiAl by first-principles calculations. *Acta. Mater* **1996**, *44*, 1471–1478. [CrossRef]

86. Zuqing, S.; Wangyue, Y.; Lizhen, S.; Yuanding, H.; Baisheng, Z.; Jilian, Y. Neutron diffraction study on site occupation of substitutional elements at sub lattices in Fe$_3$Al intermetallics. *Mater. Sci. Eng.: A* **1998**, *258*, 69–74. [CrossRef]

87. Nishino, Y.; Asano, S.; Ogawa, T. Phase stability and mechanical properties of Fe$_3$Al with addition of transition elements. *Mater. Sci. Eng.: A* **1997**, *234*, 271–274. [CrossRef]

88. Nishino, Y.; Kumada, C.; Asano, S. Phase stability of Fe$_3$Al with addition of 3d transition elements. *Scr. Mater.* **1997**, *36*, 461–466. [CrossRef]

89. Krein, R.; Schneider, A.; Sauthoff, G.; Frommeyer, G. Microstructure and mechanical properties of Fe$_3$Al-based alloys with strengthening boride precipitates. *Intermetallics* **2007**, *15*, 1172–1182. [CrossRef]

90. Connetable, D.; Lacaze, J.; Maugis, P.; Sundman, B. A calphad assessment of Al-C-Fe system with the κ carbide modelled as an ordered form of the fcc phase. *Calphad* **2008**, *32*, 361–370. [CrossRef]

91. Schneider, A.; Falat, L.; Sauthoff, G.; Frommeyer, G. Constitution and microstructures of Fe-Al-M-C (M = Ti, V, Nb, Ta) alloys with carbides and laves phase. *Intermetallics* **2003**, *11*, 443–450. [CrossRef]

92. Kobayashi, S.; Zaefferer, S.; Schneider, A. Carbide Precipitation in an Fe$_3$Al-Cr-Mo-C Alloy. In *Proceedings of an International Conference on Solid-Solid Phase Transformations in Inorganic Materials 2005, Vol. 1: Diffusional transformations*; Wiley: New York, NY, USA, 2005.

93. Doucakis, T.; Kumar, K. Formation and stability of refractory metal diborides in an Fe_3Al matrix. *Intermetallics* **1999**, *7*, 765–777. [CrossRef]

94. Morris, M.; Morris, D. Dispersoid additions and their effect on high temperature deformation of FeAl. *Acta Metall. Mater.* **1990**, *38*, 551–559. [CrossRef]

95. Palm, M. Fe-Al materials for structural applications at high temperatures: Current research at mpie. *Int. J. Mater. Res.* **2009**, *100*, 277–287. [CrossRef]

96. Risanti, D.; Deges, J.; Falat, L.; Kobayashi, S.; Konrad, J.; Palm, M.; Pöter, B.; Schneider, A.; Stallybrass, C.; Stein, F. Dependence of the brittle-to-ductile transition temperature (BDTT) on the Al content of Fe-Al alloys. *Intermetallics* **2005**, *13*, 1337–1342. [CrossRef]

97. Anthony, L.; Fultz, B. Effects of early transition metal solutes on the $D0_3$-B2 critical temperature of Fe_3Al. *Acta Metall. Mater.* **1995**, *43*, 3885–3891. [CrossRef]

98. Fleischer, R.L. Substitutional solutes in AlRu-I. Effects of solute on moduli, lattice parameters and vacancy production. *Acta Metall. Mater.* **1993**, *41*, 863–869. [CrossRef]

99. Fleischer, R.L. Substitutional solutes in AlRu-II. Hardening and correlations with defect structure. *Acta Metall. Mater.* **1993**, *41*, 1197–1205. [CrossRef]

100. Schneibel, J.; Specht, E.; Simpson, W. Solid solution strengthening in ternary B2 iron aluminides containing 3d transition elements. *Intermetallics* **1996**, *4*, 581–583. [CrossRef]

101. Zamanzade, M.; Barnoush, A. Effect of chromium on the electrochemical properties of iron aluminide intermetallics. *Corros. Sci.* **2014**, *78*, 223–232. [CrossRef]

102. Rao, V.S. A review of the electrochemical corrosion behaviour of iron aluminides. *Electrochim. Acta* **2004**, *49*, 4533–4542. [CrossRef]

103. Balasubramaniam, R. On the role of chromium in minimizing room temperature hydrogen embrittlement in iron aluminides. *Scr. Mater.* **1996**, *34*, 127–133. [CrossRef]

104. Hakiki, N. Comparative study of structural and semiconducting properties of passive films and thermally grown oxides on AISI 304 stainless steel. *Corros. Sci.* **2011**, *53*, 2688–2699. [CrossRef]

105. Rose, J.H.; Smith, J.R.; Ferrante, J. Universal features of bonding in metals. *Phys. Rev. B* **1983**, *28*, 1835. [CrossRef]

106. Rose, J.H.; Smith, J.R.; Guinea, F.; Ferrante, J. Universal features of the equation of state of metals. *Phys. Rev. B* **1984**, *29*, 2963. [CrossRef]

107. Morris, D.G.; Dadras, M.; Morris, M. The influence of chromium additions on order and ductility in Fe_3Al intermetallic. *J. Phys. IV* **1993**, *3*, C7-429–C427-434. [CrossRef]

108. Zamanzade, M.; Vehoff, H.; Barnoush, A. Effect of chromium on elastic and plastic deformation of Fe_3Al intermetallics. *Intermetallics* **2013**, *41*, 28–34. [CrossRef]

109. Zamanzade, M.; Rafael-Velayarce, J.; Torrents-Abad, O.; Motz, C.; Barnoush, A. Mechanical behavior of iron aluminides: A comparison of nanoindentation, compression and bending of micropillars. *Mater. Sci. Eng. A* **2015**. [CrossRef]

110. Barnoush, A.; Zamanzade, M. Effect of substitutional solid solution on dislocation nucleation in Fe_3Al intermetallic alloys. *Philos. Mag.* **2012**, *92*, 3257–3268. [CrossRef]

111. Motz, C.; Schoberl, T.; Pippan, R. Mechanical properties of micro-sized copper bending beams machined by the focused ion beam technique. *Acta Mater.* **2005**, *53*, 4269–4279. [CrossRef]

112. Ellinger, C.S. In situ oxidation study of flat and stepped binary alloy surfaces. Ph.D. Thesis, Institut für Theoretische und Angewandte Physik &Max-Planck-Institut für Intelligente Systeme, Stuttgart, Germany, 2010.

113. Hammer, L.; Meier, W.; Blum, V.; Heinz, K. Equilibration processes in surfaces of the binary alloy Fe-Al. *J. Phys. Condens. Matter* **2002**, *14*. [CrossRef]

114. Baddorf, A.; Chandavarkar, S. Identification of an incommensurate $FeAl_2$ overlayer on FeAl (110) using X-ray diffraction and reflectivity. *Phys. B: Condens. Matter* **1996**, *221*, 141–144. [CrossRef]

115. Voges, D.; Taglauer, E.; Dosch, H.; Peisl, J. Surface segregation on Fe_3Al (110) near the order-disorder transition temperature. *Surf. Sci.* **1992**, *269*, 1142–1146. [CrossRef]

116. Dosch, H.; Mailänder, L.; Johnson, R.; Peisl, J. Critical phenomena at the Fe_3Al (110) surface: A glancing angle X-ray scattering study. *Surf. Sci.* **1992**, *279*, 367–379. [CrossRef]

117. Hutchings, R.; Loretto, M. Compositional dependence of oxidation rates of NiAl and CoAl. *Metal Sci.* **1978**, *12*, 503–510. [CrossRef]

118. Pöter, B.; Stein, F.; Wirth, R.; Spiegel, M. Early stages of protective oxide layer growth on binary iron aluminides. *Z. Phys. Chem.* **2005**, *219*, 1489–1503. [CrossRef]

119. Velon, A.; Olefjord, I. Oxidation behavior of Ni$_3$Al and Fe$_3$Al: I. Early stage of oxide growth. *Oxid. Metals* **2001**, *56*, 425–452. [CrossRef]

120. Velon, A.; Yi, D.-Q. Influence of Cr on the oxidation of Fe$_3$Al and Ni$_3$Al at 500 °C. *Oxid. Metals* **2002**, *57*, 13–31. [CrossRef]

121. Lee, W.; Lin, R. Oxidation, sulfidation and hot corrosion of intermetallic compound Fe$_3$Al at 605 °C and 800 °C. *Mater. Chem. Phys.* **1999**, *58*, 231–242. [CrossRef]

122. Vogel, D.; Hotař, A.; Vogel, A.; Palm, M.; Renner, F.U. Corrosion behaviour of Fe-Al(-Ti) alloys in steam. *Intermetallics* **2010**, *18*, 1375–1378. [CrossRef]

123. Pint, B.A.; Wright, I.G. The Oxidation Behavior of Fe-Al Alloys. *Mater. Sci. Forum* **2004**, *461–464*, 799–806. [CrossRef]

124. Janda, D. Mechanical Properties and Oxidation Behavior of Micro-Alloyed Iron Aluminides. Ph.D. Thesis, Karlsruher Institut für Technologie (KIT), Karlsruhe, Germany, 18 February 2015.

125. Grabke, H. Oxidation of NiAl and FeAl. *Intermetallics* **1999**, *7*, 1153–1158. [CrossRef]

126. Kim, I.; Cho, W.D.; Kim, H.J. High-temperature oxidation of Fe$_3$Al containing yttrium. *J. Mater. Sci.* **2000**, *35*, 4695–4703. [CrossRef]

127. Frangini, S.; Giorgi, R.; Lascovich, J.; Mignone, A. XPS study of passive films formed on an iron-aluminium intermetallic compound in acid solution. *Surf. Interface Anal.* **1994**, *21*, 435–441. [CrossRef]

128. McCafferty, E. Thermodynamics of corrosion: Pourbaix diagrams. In *Introduction to Corrosion Science*; Springer: Berlin, Germany, 2010; pp. 95–117.

129. De Cristofaro, N.; Frangini, S.; Mignone, A. Passivity and passivity breakdown on a β-FeAl intermetallic compound in sulphate and chloride containing solutions. *Corros. Sci.* **1996**, *38*, 307–315. [CrossRef]

130. Frangini, S.; De Cristofaro, N.; Lascovich, J.; Mignone, A. On the passivation characteristics of a β-FeAl intermetallic compound in sulphate solutions. *Corros. Sci.* **1993**, *35*, 153–159. [CrossRef]

131. Moshier, W.; Davis, G.; Ahearn, J. The corrosion and passivity of aluminum exposed to dilute sodium sulfate solutions. *Corros. Sci.* **1987**, *27*, 785–801. [CrossRef]

132. George, F.O. Chromium-Free Conversion Coating of Aluminium-Copper Alloys. Ph.D. Thesis, The University of Manchester, Manchester, UK, 4 February 2011.

133. Vargel, C. *Corrosion of Aluminium*; Elsevier: Amsterdam, The Nietherlands, 2004.

134. García-Alonso, M.C.; López, M.F.; Escudero, M.L.; González-Carrasco, J.L.; Morris, D.G. Corrosion behaviour of an Fe$_3$Al-type intermetallic in a chloride containing solution. *Intermetallics* **1999**, *7*, 185–191. [CrossRef]

135. Rosalbino, F.; Carlini, R.; Parodi, R.; Zanicchi, G.; Scavino, G. Investigation of passivity and its breakdown on Fe$_3$Al-Si and Fe$_3$Al-Ge intermetallics in chloride-containing solution. *Corros. Sci.* **2014**, *85*, 394–400. [CrossRef]

136. Johnson, W.H. On some remarkable changes produced in iron and steel by the action of hydrogen and acids. *Proc. R. Soc. Lond.* **1874**, *23*, 168–179. [CrossRef]

137. Lynch, S. Comments on "a unified model of environment-assisted cracking". *Scr. Mater.* **2009**, *61*, 331–334. [CrossRef]

138. Gangloff, R.P.; Somerday, B.P. *Gaseous Hydrogen Embrittlement of Materials in Energy Technologies: Mechanisms, Modelling and Future Developments*; Elsevier: Amsterdam, The Nietherlands, 2012; Volume 2.

139. McKamey, C.; Liu, C. Chromium addition and environmental embrittlement in Fe$_3$Al. *Scr. Metall. Mater.* **1990**, *24*, 2119–2122. [CrossRef]

140. Stroe, M.E. Hydrogen Embrittlement of Ferrous Materials. Ph.D. Thesis, Universite Libre De Bruxelles, Brussel, Belgium, 31 March 2006.

141. Fu, C.; Painter, G. First principles investigation of hydrogen embrittlement in FeAl. *J. Mater. Res.* **1991**, *6*, 719–723. [CrossRef]

142. Johnson, D.F.; Carter, E.A. First-principles assessment of hydrogen absorption into FeAl and Fe$_3$Si: Towards prevention of steel embrittlement. *Acta Mater.* **2010**, *58*, 638–648. [CrossRef]

143. Hirth, J.P. Effects of hydrogen on the properties of iron and steel. *Metall. Trans. A* **1980**, *11*, 861–890. [CrossRef]

144. Cheng, X.; Wan, X. Hydrogen diffusivity in a Fe$_3$Al-based alloy. *Scr. Mater.* **1998**, *38*, 1505–1509. [CrossRef]

145. Kupka, M.; Stępień, K. Hydrogen permeation in Fe-40at.% Al alloy at different temperatures. *Corros. Sci.* **2009**, *51*, 699–702. [CrossRef]

146. Banerjee, P.; Balasubramaniam, R. Hydrogen diffusivity in iron aluminides determined by subscale microhardness profiling. *Scr. Mater.* **1998**, *39*, 1215–1219. [CrossRef]

147. Yang, Y.; Hanada, S. Absorption and desorption of hydrogen in Fe-40Al intermetallic. *Scr. Metall. Mater.* **1995**, *32*, 1719–1724. [CrossRef]

148. Luu, W.; Wu, J. Hydrogen transport and environmental embrittlement effects in iron aluminides. *J. Mater. Sci.* **2000**, *35*, 4121–4127. [CrossRef]

149. Stępień, K.; Kupka, M. Diffusivity of hydrogen in B2 iron aluminides. *Scr. Mater.* **2006**, *55*, 585–588. [CrossRef]

150. Prakash, U.; Parvathavarthini, N.; Dayal, R. Effect of composition on hydrogen permeation in Fe-Al alloys. *Intermetallics* **2007**, *15*, 17–19. [CrossRef]

151. Kimizuka, H.; Mori, H.; Ogata, S. Effect of temperature on fast hydrogen diffusion in iron: A path-integral quantum dynamics approach. *Phys. Rev. B* **2011**, *83*, 094110. [CrossRef]

152. Bockris, J.M.; Fullenwider, M. The electro-permeation of hydrogen into metals. *Electrochim. Acta* **1970**, *15*, 47–60. [CrossRef]

153. Song, R.H.; Pyun, S.; Oriani, R. Hydrogen permeation through the passivation film on iron by time-lag method. *J. Electrochem. Soc.* **1990**, *137*, 1703–1706. [CrossRef]

154. Ruetschi, P.; Giovanoli, R. Cation vacancies in MnO_2 and their influence on electrochemical reactivity. *J. Electrochem. Soc.* **1988**, *135*, 2663–2669. [CrossRef]

155. Song, R.-H.; Pyun, S.-I.; Oriani, R. The hydrogen permeation through passivating film on iron by modulation method. *Electrochim. Acta* **1991**, *36*, 825–831. [CrossRef]

156. Zhang, G.; Wang, X.; Yang, F.; Shi, Y.; Song, J.; Lai, X. Energetics and diffusion of hydrogen in hydrogen permeation barrier of α-Al_2O_3/ FeAl with two different interfaces. *Int. J. Hydrog. Energy* **2013**, *38*, 7550–7560. [CrossRef]

157. Hollenberg, G.; Simonen, E.; Kalinin, G.; Terlain, A. Tritium/hydrogen barrier development. *Fusion Eng. Des.* **1995**, *28*, 190–208.

158. Barnoush, A.; Vehoff, H. Hydrogen embrittlement of aluminum in aqueous environments examined by *in situ* electrochemical nanoindentation. *Scr. Mater.* **2008**, *58*, 747–750. [CrossRef]

159. Pundt, A.; Kirchheim, R. Hydrogen in metals: Microstructural aspects. *Annu. Rev. Mater. Res.* **2006**, *36*, 555–608. [CrossRef]

160. Myers, S.M.; Baskes, M.; Birnbaum, H.; Corbett, J.W.; De Leo, G.; Estreicher, S.; Haller, E.E.; Jena, P.; Johnson, N.M.; Kirchheim, R. Hydrogen interactions with defects in crystalline solids. *Rev. Mod. Phys.* **1992**, *64*, 559–617. [CrossRef]

161. Ryu, J.H. Hydrogen Embrittlement in Trip and Twip Steels. Ph.D. Thesis, Pohang University of Science and Technology, Pohang, South Korea, 29 May 2012.

162. Myers, S.; Besenbacher, F.; No, J. Immobilization mechanisms for ion-implanted deuterium in aluminum. *J. Appl. Phys.* **1985**, *58*, 1841–1850. [CrossRef]

163. Ziegler, R.; Schaefer, H. Vacancies and interstitials in metals and alloys. In Proceedings of the 1987 International Conference on Vacancies and Interstititials in Metals and Alloys, Berlin, Germany, 14–19 September 1987.

164. Linderoth, S.; Rajainmäki, H.; Nielsen, B.; Hansen, H.; Nieminen, R.M.; Petersen, K. Hydrogen in Vacancies in Mo and Ni. *Mater. Sci. Forum* **1987**, *15–18*, 751–756. [CrossRef]

165. Wittmann, M.; Wu, D.; Baker, I.; George, E.; Heatherly, L. The role of edge and screw dislocations on hydrogen embrittlement of Fe-40Al. *Mater. Sci. Eng.: A* **2001**, *319*, 352–355. [CrossRef]

166. Tien, J.; Thompson, A.W.; Bernstein, I.; Richards, R.J. Hydrogen transport by dislocations. *Metall. Trans. A* **1976**, *7*, 821–829. [CrossRef]

167. Louthan, M.; Caskey, G.; Donovan, J.; Rawl, D. Hydrogen embrittlement of metals. *Mater. Sci. Eng.* **1972**, *10*, 357–368. [CrossRef]

168. Donovan, J.A. Accelerated evolution of hydrogen from metals during plastic deformation. *Metall. Trans. A* **1976**, *7*, 1677–1683. [CrossRef]

169. Nathal, M.; Liu, C. Intrinsic ductility of FeAl single crystals. *Intermetallics* **1995**, *3*, 77–81. [CrossRef]

170. Lynch, R.; Gee, K.; Heldt, L. Environmental embrittlement of single crystal and thermomechanically processed B2-ordered iron aluminides. *Scr. Metall. Mater.* **1994**, *30*, 945–950. [CrossRef]
171. Saka, H.; Nishizaki, T. Roles of edge and screw dislocations in the environmental embrittlement of an Fe [sbnd] Al intermetallic compound. *Philos. Mag. A* **1996**, *73*, 1173–1179. [CrossRef]
172. Yang, Y.; Baker, I.; George, E. Effect of vacancies on the tensile properties of Fe-40Al single crystals in air and vacuum. *Mater. Charact.* **1999**, *42*, 161–167. [CrossRef]
173. Munroe, P.; Baker, I. Observation of <001> dislocations and a mechanism for transgranular fracture on {001} in FeAl. *Acta Metall. Mater.* **1991**, *39*, 1011–1017. [CrossRef]
174. Li, J.; Liu, C. Crack nucleation in hydrogen embrittlemet. *Scr. Metall. Mater.* **1992**, *27*, 1701–1705. [CrossRef]